Revision 1

1   **Constraints on the origin of sub-effusive nodules from the Sarno (Pomici di Base) eruption**
2   **of Mt. Somma-Vesuvius (Italy) based on compositions of silicate-melt inclusions and**
3   **clinopyroxene**

4   **Rita Klébesz[1,2,*], Rosario Esposito[1,2], Benedetto De Vivo[2] and Robert J. Bodnar[1]**
5   [1]Department of Geosciences, Virginia Polytechnic Institute and State University, Blacksburg,
6   Virginia 24061, U.S.A.
7   [2]Dipartimento di Scienze della Terra, dell'Ambiente e delle Risorse, Università di Napoli
8   "Federico II", Naples, 80134, Italy
9   [*]Present address: MTA CSFK Geodetic and Geophysical Institute, Sopron, 9400, Hungary, e-
10 mail: klebesz.rita@csfk.mta.hu

11

12   **Abstract**

13 Major and trace element and volatile compositions of reheated melt inclusions (RMI) and their

14 clinopyroxene hosts from a selected "sub-effusive" nodule from the uppermost layer of the Sarno

15 (Pomici di Base; PB) plinian eruption of Mt. Somma-Vesuvius (Italy) have been determined.

16 The Sarno eruption occurred during the first magmatic mega-cycle and is one of the oldest

17 documented eruptions at Mt. Somma-Vesuvius. Based on MI and clinopyroxene composition we

18 constrain processes associated with the origin of the nodule, its formation depth, and hence the

19 depth of the magma chamber associated with the Sarno (PB) eruption. The results contribute to a

20 better understanding of the early stages of evolution of long-lived Mt. Somma-Vesuvius volcanic

21 complex.

22   The crystallized MI were heated to produce a homogeneous glass phase prior to analysis. MI

23 homogenized between 1202-1256 °C, and three types of RMI were distinguished based on their

24 compositions and behavior during heating. Type I RMI is classified as phono-tephrite – tephri-

25 phonolite – shoshonite, and is the most representative of the melt phase from which the

26 clinopyroxenes crystallized. The second type, referred to as basaltic RMI, have compositions that

27 have been modified by accidentally trapped An-rich feldspar and/or by overheating during

28 homogenization of the MI. The third type, referred to as high-P RMI, is classified as picro-basalt

29 and has high-P content due to accidentally trapped apatite.

30   Type I RMI are more representative of magmas associated with pre-Sarno eruptions than to

31   magma associated with the Sarno (PB) eruption based on published bulk rock compositions for

32   Mt. Somma-Vesuvius. Therefore, it is suggested that the studied nodule formed from a melt

33   compositionally similar to that which was erupted during the early history of Mt. Somma. The

34   clinopyroxene and clinopyroxene-silicate melt thermobarometer models suggest minimum

35   pressures of 400 MPa (~11 km) for nodule formation, which is greater than pressures and depths

36   commonly reported for the magmas associated with younger plinian eruptions of Mt. Somma-

37   Vesuvius. Minimum pressures of formation based on volatile concentrations of MI interpreted

38   using H_2O-CO_2-silicate melt solubility models indicate formation pressures $\leq$300 MPa.

39   **Keywords:** melt inclusion, homogenization, thermobarometer, Mt. Somma-Vesuvius, nodule,

40   volcanic risk

41

42   **Introduction**

43   Volcanic activity at Mt. Somma-Vesuvius (Campanian Plain, South Italy) has been the focus of

44   volcanological research for at nearly two millennia, starting with the letters written by Pliny the

45   Younger describing the eruption of Mt. Somma in 79 AD that destroyed Pompeii and killed his

46   uncle, Pliny the Elder. This work has been motivated not only by scientific curiosity but also, in

47   more recent years, by the significant volcanic hazard posed by the proximity of Mt. Somma-

48   Vesuvius to the densely populated city of Naples.

49   While Mt. Somma – Vesuvius has been active for more than 25 ka, most research has

50   focused on the products of the post-79 AD eruptions. The research focused both on the juvenile

51   products (Ayuso et al. 1998; Barberi et al. 1981; Belkin et al. 1993, 1998; Black et al. 1998;

52   Cioni 2000; Cioni et al. 1995, 1998; Civetta et al. 1991; Fulignati and Marianelli 2007; Joron et

53   al. 1987; Lima et al. 1999; Marianelli et al. 1995, 1999, 2005; Marini et al. 1998; Mastrolorenzo

54   et al. 1993; Mues-Schumacher 1994; Paone 2006, 2008; Piochi et al. 2006a; Raia et al. 2000;

55   Rolandi et al. 1993; Rosi and Santacroce 1983; Santacroce et al. 1993, 2008; Schiano et al. 2004;

56   Somma et al. 2001; Vaggelli et al. 1993; Villemant et al. 1993; Webster et al. 2001) and on the

57   co-genetic or xenolithic lithic fragments, referred to as nodules (Barberi and Leoni 1980; Belkin

58   and De Vivo 1993; Belkin et al. 1985; Cioni et al. 1995; Cundari 1982; Del Moro et al. 2001;

59   Fulignati and Marianelli 2007; Fulignati et al. 1998, 2001, 2004, 2005; Gilg et al. 2001; Hermes

60   and Cornell 1978, 1981; Lima et al. 2003, 2007; Savelli 1968; Sorby 1858). As a result of these

61   studies, the composition of the source region, the structure of the plumbing system, and the pre-

62   eruptive processes and volatile contents of the magmas are fairly well constrained for the post-79

63   AD eruptions. However, less attention has been devoted to the older eruptions. While abundant

64   data are available for the whole rock compositions of the juvenile products, much less

65   information is available for the melt inclusions (MI).

66   MI can provide valuable information concerning melt generation and evolution, and the

67   trapping conditions for the MI (Anderson 2003). In addition, MI represent the only tool that can

68   directly provide the pre-eruptive volatile (such as H_2O, CO_2, S, Cl, F) content of a magma. The

69   bulk rock measurements only provide a minimum estimate of volatiles at depth owing to

70   continued degassing during ascent and emplacement on the surface (Lowenstern 2003). In

71   addition, MI from nodules may provide important information related to igneous processes

72   occurring at the magma-country rock interface (e.g., De Vivo et al. 2006).

73   This study focuses on a sub-effusive nodule (NLM1-1a) previously described by (Klébesz et

74   al. 2012). They reported preliminary results (major and trace element compositions) of MI

75   obtained by analyses of crystallized, unexposed MI using Laser Ablation Inductively-Coupled

76   Plasma Mass Spectrometry (LA-ICP-MS). This method, however, does not provide information

77   on the volatile content, and the formation P and T cannot be constrained due to large

78   uncertainties in the major element content associated with analyzing crystallized MI. By heating

79   and homogenizing the MI in the clinopyroxenes, we were able to overcome these obstacles.

80   Major and minor element concentrations of 132 RMI were obtained by Electron Microprobe

81   Analysis (EPMA), trace element concentrations of 73 RMI by LA-ICP-MS, and volatile element

82   concentrations of 32 RMI by Secondary Ion Mass Spectrometry (SIMS). Although

83   homogenization experiments have some disadvantages owing to possible overheating and/or host

84   assimilation, variations related to natural processes and those associated with the heating

85   experiments can often be distinguished. In addition, the obtained data can be used to estimate the

86   formation conditions (P, T) of the MI, hence the depth at which the nodule originated or last

87   equilibrated. The results of this study provide constraints that help us to better understand the

88   early stages of evolution of the Mt. Somma-Vesuvius volcanic complex.

89

90   **Geological background**

91   During the Quaternary period, potassium-rich volcanism developed in central and southern Italy,

92   forming the Roman Co-magmatic Province (Washington 1906) located along the Tyrrhenian

93   margin. The Mt. Somma-Vesuvius volcanic complex is a stratovolcano situated at the

94   southernmost end of the Roman Province, south of the Campanian Plain. The most recent review

95   by De Vivo et al. (2010) summarizes our current knowledge about the source region, plumbing

96   system and volcanic activity of Mt. Somma-Vesuvius, and here we describe the eruptive history

97   briefly.

98   Eruptive activity associated with the Mt. Somma-Vesuvius volcanic complex started after the

99   highest magnitude eruption in the Campanian Magmatic Province, the Campanian Ignimbrite

100   eruption (39 ka; De Vivo et al. 2001). Other volcanic activity in the area dates back to *ca.* 400 ka

101   (Brocchini et al. 2001; De Vivo et al. 2001; Rolandi et al. 2003; Santacroce et al. 2008 and

102   references therein).

103   The Mt. Somma-Vesuvius bulk rock compositions define three groups, i.e., three mega-

104   cycles (Arnó et al. 1987; Ayuso et al. 1998; Civetta and Santacroce 1992). In the following, the

105   eruptive history is described according to Rolandi (1997), and in parenthesis the names of

106   eruptions according to Santacroce (1987) are listed. The first mega-cycle lasted from >25 ka to

107   about 14 ka, and includes the older Somma activity, the Codola, the Sarno (Pomici di Base; PB),

108   and the Novelle (Verdoline) plinian eruptions and the subsequent interplinian stages. The second

109   mega-cycle started around 8 ka and lasted until about 2.7 ka, incorporating the Ottaviano

110   (Mercato) and Avellino plinian eruptions and protohistoric interplinian activity. The third mega

111   cycle started in 79 AD with the Pompeii plinian eruption and the subsequent ancient historical

112   interplinian activity. Two other subplinian eruptions belong to this mega-cycle; the 472 AD

113   (Pollena) and the 1631 AD eruptions, both followed by interplinian activity. The last eruption

114   occurred in 1944 and either represents the end of the most recent mega-cycle or simply one of

115   the many eruptions within the continuing third mega-cycle, which would represent an unusually

116   long repose time between eruptions within the continuing third mega-cycle (De Vivo et al. 2010

117   and references therein).

118   The products of the first mega-cycle are slightly silica-undersaturated (K-trachyte, K-latite;

119   e.g., Ayuso et al. 1998; Paone 2006; Piochi et al. 2006a; Santacroce et al. 2008). The products of

120   the second mega-cycle are mildly silica-undersaturated (phonotephrites to phonolites; e.g.,

121 Ayuso et al. 1998; Piochi et al. 2006a; Santacroce et al. 2008). The third mega-cycle is

122 characterized by strongly silica-undersaturated rocks with tephrite to tephriphonolite-foidite

123 composition (e.g., Ayuso et al. 1998; Piochi et al. 2006a; Santacroce et al. 2008).

124

125 **Previous studies on nodules from Mt. Somma-Vesuvius**

126 In the Mt. Somma-Vesuvius literature, the term nodule refers to ejecta showing wide

127 variability in composition and texture that are common in the pyroclastic products. Nodules can

128 be metamorphic and/or metasomatized sedimentary rocks, ranging from carbonates to silicic

129 skarn rocks, as well as coarse-grained igneous rocks and cumulate rocks. Zambonini (1910) was

130 the first to describe nodules in the Mt. Somma-Vesuvius deposits, but the classification which

131 has been used recently was proposed by Hermes and Cornell (1978). They divided the Mt.

132 Somma-Vesuvian nodules into four groups: 1) ultramafic cumulates, 2) "skarns", representing

133 metasomatized carbonates, 3) recrystallized carbonate hornfels, and 4) "sub-effusive" rocks,

134 which are shallow plutonic rocks.

135 In the Mt. Somma-Vesuvius system, the earlier studies focused on constraining the physical

136 parameters of nodule genesis, but did not consider the geochemical or petrological origin of the

137 nodules or whether they are co-genetic with their pyroclastic hosts. Sorby (1858) studied

138 metasomatized carbonate (skarn) ejecta and concluded that the minerals formed between 340 and

139 380 °C and at a depth of about 0.6-1 km. Barberi and Leoni (1980) also studied skarns, but they

140 assumed a temperature range of 360-790 °C and a maximum depth of 5-6 km. Cortini et al.

141 (1985) estimated the crystallization temperature of phenocrysts in skarns to be 850-1050 °C, and

142 1170-1240 °C in cumulates, based on the homogenization temperatures of MI. Belkin and De

143 Vivo (1993) and Belkin et al. (1985) suggested a multistage crystallization history, based on the

6

144   bimodal distribution of CO_2 fluid inclusion (FI) densities, and estimated 3.5-13 km and 4-10 km

145   for the depth of nodule formation for the interplinian and the plinian eruptions, respectively.

146   Belkin and De Vivo (1993) also noted that FI in nodules from the plinian eruption have higher

147   H_2O-content compared to those from the inter-plinian eruption.

148   The origin and genesis of the nodules from Mt. Somma-Vesuvius has been controversial.

149   Based on the mineral assemblages and the interstitial glass compositions, Hermes and Cornell

150   (1981, 1983) inferred that the cumulate nodules formed over a range of depths, with a maximum

151   pressure of 300 MPa (~8 km). But, Varekamp (1983) argued that all nodules were derived from

152   the same, shallow source. Savelli (1968) examined carbonate ejecta and concluded, based on the

153   non-equilibrium assemblages, that there was no direct evidence of wall rock assimilation but

154   rather that metasomatism by volcanic fluids and gases was responsible for the observed

155   compositions. Today, it is generally accepted that the silicate crystalline nodules and the skarns

156   represent samples of the heterogeneous wallrock of the magma chamber. The large

157   compositional variations reflect the gradual changes from the carbonate country rock through

158   skarns and metasomatized cumulate rocks to a cumulate crystal mush along the inner walls of the

159   chamber (Cioni et al. 1995). Little information is available about the origin of sub-effusive type

160   nodules that were reported by Hermes and Cornell (1978) from several different eruptions. Most

161   commonly, sub-effusive nodules are interpreted as representing shallow plutonic rocks that

162   usually show compositions equivalent to the erupted lavas or pyroclastics (Belkin and De Vivo

163   1993; Hermes and Cornell 1978) or intermediate between lava and cumulate compositions

164   (Hermes and Cornell 1978). Hermes and Cornell (1978) suggested that sub-effusive nodules

165   represent the crystal rich part of the crystal mush zone, but this hypothesis was never tested.

166   Many studies have focused on skarn and silicic nodules from post 79 AD plinian eruptions to

167   understand processes occurring at the magma/wall rock interface and to constrain the underlying

168   plumbing system of the volcano. These studies (Del Moro et al. 2001; Fulignati et al. 1998,

169   2000, 2001, 2004, 2005; Gilg et al. 2001) concluded that skarn generation can be explained by

170   carbonate wall rock assimilation by mafic alkaline magma that leads to the exsolution of CO_2-

171   rich vapor and complex saline melts from the contaminated magma. These fluids react with the

172   carbonate wall rock resulting in skarn formation. All of the above studies estimate a high

173   (magmatic) temperature, above 700 °C, for skarn formation.

174   Lima et al. (2003, 2007) constrain the post 79 AD evolution of Mt. Somma-Vesuvius based

175   on compositional data from FI and MI trapped in crystals of nodules. According to their model,

176   separate small magma chambers exist at depths of >3.5 km and possibly a larger chamber is

177   present at a depth of >12 km. In this model, interplinian periods represent a steady state

178   condition under the volcano. During these periods, the volcano acts like an "open system",

179   indicating that the input of a new supply of magma is always followed by eruption. However, at

180   the end of these periods, cooling of the magma leads to the precipitation of newly formed

181   crystals, which subsequently leads to self-sealing, and hence "closing" of the system. In this

182   situation, the pressure can build up, leading to a subsequent highly explosive plinian eruption. It

183   was also suggested that a carapace forms around the upper portion of the shallow magma

184   chamber (3.6-4.5 km) and acts as an interface between the brittle and plastic rocks (Lima et al.

185   2007).

186   Klébesz et al. (2012) studied sub-effusive nodules from the ~20 ka Sarno (PB) eruption.

187   Their study focused mainly on the petrography and mineral chemistry of the nodules. They also

188   reported MI in clinopyroxene. Klébesz et al. (2012) distinguished two types of MI based on

189   petrography, and their classification was supported by compositions determined by LA-ICP-MS.

190   Type I MI contain mica, Fe-Ti-oxide phases and/or dark green spinel, clinopyroxene, feldspar

191   and a vapor bubble. Type II inclusions are generally lighter in color, compared to type I MI,

192   when observed in transmitted light. Generally, Type II MI contain subhedral feldspar, glass,

193   oxides and/or one or more bubbles. Type I MI are classified as phono-tephrite – tephri-phonolite

194   – basaltic trachy-andesite, while Type II MI have basaltic composition (Klébesz et al. 2012).

195   Based on the texture of the nodules and the composition of the minerals and MI, they proposed

196   that the studied nodules originated from crystal-rich mush zones within the plumbing system of

197   Mt. Somma-Vesuvius. In addition, Klébesz et al. (2012) reported that data from crystallized MI

198   suggest magma heterogeneities during the early stages of this volcanic system.

199

200   **Description of samples and methods**

201   Nodules were collected from the uppermost layer of the Sarno eruption in the Traianello quarry,

202   located on the NE slope of Mt. Somma. The nodules consist of An-rich plagioclase, K-feldspar,

203   clinopyroxene (ferro-diopside), mica (phlogopite-biotite) ± olivine and amphibole and have a

204   porphyrogranular texture. The phenocrysts are large (up to few mm) and show variable

205   compositional zoning. Often irregular intergrowths of alkali feldspar and plagioclase with

206   clinopyroxene, mica and Fe-Ti-oxide minerals are observed. These features are interpreted as

207   crystallized melt pockets. For more detailed information on location of the collected samples,

208   petrographic description and geochemistry of the minerals in the nodule described in this study

209   (NLM1-1a) refer to Type A nodules in Klébesz et al. (2012).

210   Heating experiments on 67 clinopyroxene crystals from sample NLM1-1a were carried out in

211   the Linkam TS1400 XY heating stage. The specifications of the heating stage and the details of a

9

212 heating experiment are discussed by Esposito et al. (2012). Heating experiments were conducted

213 during five analytical sessions. In every crystal one MI was preselected and observed

214 continuously and photographed at various times (temperatures) during the heating experiment

215 (Deposit Item-01). Heating was continued until the observed inclusion homogenized, then the

216 sample was quenched. Subsequently, the host crystals were individually mounted in epoxy and

217 polished until the reheated melt inclusion (RMI) was exposed (Thomas and Bodnar 2002). The

218 crystals were removed from the epoxy by a hot needle, and then they were cleaned in distilled

219 water and mounted in a one-inch diameter indium probe mount. A 5 nm evaporative gold coating

220 was applied for the Scanning Electron Microscope (SEM) and for EPMA, and a 30 nm thick

221 sputtered gold coating was applied for SIMS to minimize C-contamination (see Esposito et al.

222 2014).

223 Reheated MI (RMI) were analyzed for major and minor elements (SiO_2, TiO_2, Al_2O_3, FeO,

224 MnO, MgO, CaO, Na_2O) by EPMA and for trace elements (Sc, V, Cr, Ni, Rb, Sr, Y, Zr, Nb, Ba,

225 La, Ce, Nd, Sm, Eu, Yb) by LA-ICP-MS. Sample preparation and the specifications of the

226 analytical methods are identical to those described in Klébesz et al. (2012).

227 RMI were analyzed for volatile (H_2O, CO_2, F, Cl, S) abundances using the SIMS 7f GEO ion

228 probe at Virginia Tech. Analyses were performed using $^{133}Cs^+$ as the source, with a current

229 between 1 and 1.6 nA. A 30 μm x 30 μm spot was rastered within the glass for 240 s to clean

230 the surface before analysis. Then, a 15 μm x 15 μm spot within the rastered area was analyzed

231 using 15 accumulations in depth profile mode. Volatile contents were related to the ratio of the

232 isotope (mass) of interest ($^{16}O^1H$, ^{12}C, ^{19}F, ^{32}S or ^{35}Cl) to ^{30}Si. Four natural standard glasses were

233 used to calibrate the SIMS (EN11346D-2, ALV1649-3, GL07D52-5 and ALV1654-3; Helo et al.

234 2011). The measured element ratios (e.g., $^{12}C/^{30}Si$) were plotted against the known volatile

10

235 concentration (e.g., CO_2) of the standard glasses to define the calibration curve. In addition, it

236 has to be emphasized that in some cases the volatile concentration (usually F and sometimes Cl)

237 of the sample was too high and saturated the Faraday cup, therefore, the concentrations of those

238 volatile species could not be determined. Calibration curves used in this study are reported by

239 Esposito et al. (2014) in the deposit items for working session October 2011.

240   The estimated standard deviation (e.s.d.; 1 sigma) of the EPMA is usually below 5%, if the

241 concentration is above 1 wt%. The e.s.d. (3 sigma) of the LA-ICP-MS analysis was calculated

242 based on Longerich et al. (1996). The 1σ errors based on the slope of each calibration line are

243 5% relative for CO_2, 3% for H_2O and F, 6% for S, and 1% for Cl [see Deposit item AM-14-508,

244 Octeber_2011 working session in Esposito et al. (2014)]. Based on multiple analyses of three

245 standard glasses, the 1σ reproducibility is 5% for H_2O and F, 6% for S, 14% for CO_2, and 24%

246 for Cl in average. Esposito et al. (2014) analyzed groups of MI all trapped at the same time (melt

247 inclusion assemblage) and estimated SIMS uncertainties of ~10-15% for H_2O and Cl and ~10%

248 for F. It is important to note that Esposito et al. (2014) reported that MI within a single melt

249 inclusion assemblage show large variability for CO_2 and S concentrations that is beyond the

250 SIMS analytical error and likely due to heterogeneity within the MI.

251

252   **Results**

253 **Clinopyroxene chemistry**

254 Clinopyroxenes are present as phenocrysts and in the groundmass of the nodule. Clinopyroxene

255 compositions show some variability, but most can be classified as ferroan diopside based on the

256 compositions obtained by EPMA (Table 1 and Table 1 in Deposit Item-02). Complex

257 compositional zoning is not common in this sample, but normal zoning is occasionally observed.

11

258   The MgO content of the clinopyroxene shows only moderate variation, and the calculated mg#

259   [Mg/(Mg+Fe^{total})] ranges between 0.72 and 0.82 (Table 1). No strong correlation was observed

260   between MgO and Cr (Fig. 1b), but in general, clinopyroxenes with higher MgO content tend to

261   have higher Cr concentration, showing up to ~1,300 ppm Cr in some crystals. The MgO content

262   correlates negatively with TiO_2 and Al_2O_3 contents (Fig. 1d), and also with most REE and HFSE

263   (e.g., Zr, Nb). The CaO/Al_2O_3 ratio shows good positive correlation with MgO content (Fig. 1c).

264   Some variation in the trace element concentration is observed, but all samples show similar trace

265   element patterns. The trends defined by major and trace elements and trace element patterns of

266   clinopyroxenes are consistent with fractional crystallization.

267   **Melt inclusions in clinopyroxene**

268   MI in clinopyroxene from the NLM1-1a nodule are either randomly distributed in the crystals or

269   occur along a growth zone that defines a MI assemblage (Bodnar and Student 2006) and are

270   interpreted to be primary (Roedder 1979; Sobolev and Kostyuk 1975). The MI are usually 20-30

271   μm in maximum dimension, but range from about 5 to 60 μm, and have prismatic shape. They

272   are partially to completely crystallized, indicating (relatively) slow cooling (Roedder 1979). We

273   observed two types of MI, similar to those described by Klébesz et al. (2012).

274   The homogenization temperature (T_h) of MI in clinopyroxene ranges from 1202 to 1256 °C,

275   but most of the MI show T_h between 1220-1250 °C. However, some other (smaller) MI that were

276   not monitored continuously during heating may have homogenized before the larger MI that

277   were monitored continuously and quenched after homogenization. The T_h does not necessarily

278   equal the trapping temperature (T_t) of the MI. Therefore, if the T_h is below the T_t, the MI can be

279   depleted in the host mineral components, instead if the T_h is above the T_t then the MI can be

280   enriched in those components. However, ratios of elements that are incompatible with the host

12

281 and elements showing similar concentrations in the melt and the host (e.g., TiO_2, SiO_2, La, Ce,

282 Eu, Zr.) should not be affected significantly by quenching the MI at a Th different from T_t (Lima

283 et al. 2003).

284   For crystallized MI that were analyzed by LA-ICP-MS, it was always possible to determine

285 if the analyzed MI belongs to Type I or Type II based on petrography (Klébesz et al. 2012). In

286 this study, usually one or a small number of MI in each crystal were documented and

287 photographed before the heating experiment, and these MI were monitored continuously during

288 heating to homogenization. However, after heating and then further polishing of the sample to

289 expose the target MI, additional MI that could be analyzed but which had not been documented

290 before heating were often observed. Thus, no record was available for the phases and appearance

291 of these MI before heating. Therefore, we were unable to assign some RMI to the classification

292 of Klébesz et al. (2012) using petrographic data, but instead we classify the RMI based on

293 chemical composition (Table 2 and Table 2 in Deposit Item-02). Thus, RMI with total alkali

294 content >5 wt% are classified as *Type I RMI* (Fig. 2), due to the fact that they have compositions

295 similar to Type I MI in Klébesz et al. (2012). Based on the calculated mg# of the clinopyroxene

296 which would be in equilibrium with the RMI and the measured mg# of the host, only Type I

297 RMI are in, or close to, equilibrium with the clinopyroxene host (Putirka 2008).

298   A large number (25) of RMI had alkali, silica and trace element contents that were lower

299 than Type I RMI. Here, we refer to these RMI as *basaltic RMI*, owing the fact that they are

300 classified as basalts on the total alkali silica diagram (Fig. 2; Le Bas et al. 1986). No petrographic

301 observations before heating are available for most of the basaltic RMI, but a few (5) are similar

302 to those that were classified as Type II by (Klébesz et al. 2012) based on petrography. Basaltic

303 RMI are usually small (≤20 μm) compared to type I RMI.

13

304   Some RMI with picro-basaltic composition (Fig. 2) and with high P_2O_5 (up to 8 wt%)

305   coupled with high CaO/Na_2O ratio (up to 7) were also observed, referred to here as *high-P RMI*.

306   Similar to the basaltic RMI, pre-heating petrographic information was available only for a few

307   high-P RMI. Those high-P RMI are similar to MI that were classified as Type II (Klébesz et al.

308   2012) based on petrography. Some of the high-P RMI did not homogenize completely, in some

309   cases a small solid phase, that was not large enough to be analyzed, was observed after

310   quenching. This solid phase fluoresced under the focused electron beam. These characteristics

311   suggest that the inclusions trapped silicate melt plus apatite. We have corrected the high-P RMI

312   compositions by subtracting the apatite contribution (using the stoichiometric formula

313      $Ca_5[PO_4]_3OH$) and assuming that the melt contained 0.8 wt% P_2O_5, which is the average P

314   content of Type I RMI, and any P in excess of this value is from trapped apatite. The corrected

315   compositions of the high-P RMI become similar to other RMI.

316   RMI that are petrographically similar to Type II MI reported by Klébesz et al. (2012) were

317   heated to ~1250 °C during homogenization experiments. These MI appear to homogenize to a

318   silicate melt during heating; however, after quenching and exposing them on the surface of the

319   crystals, these MI were analyzed using the SEM and classified as not having homogenized. A

320   tabular mineral phase surrounded by melt was observed. Some of these mineral phases show

321   plagioclase composition based on EPMA. Sometimes the analyzed phases were smaller than the

322   analytical volume (area) of the EPMA, therefore some of the surrounding material was included

323   in the analysis, resulting in elevated MgO, FeO and lower Al_2O_3 content. We interpret these

324   results as an indication that the MI trapped a plagioclase crystal along with melt and we will

325   refer hereafter to these MI as *Feldspar (Fsp), or fsp-bearing RMI* (Fig. 2).

14

326   RMI data show considerable scatter, but general trends are recognizable in the case of Type I

327   RMI when plotted on MgO *vs.* major oxide and trace element variation diagrams (selected

328   diagrams are shown in Fig. 3a-c). The data show an increase in SiO_2, Al_2O_3, K_2O and also in

329   P_2O_5 and Na_2O, and a decrease in CaO and FeO, with decreasing MgO, but no trend in MgO *vs.*

330   TiO_2. Most of the RMI trace elements (Rb, Sr, Zr, Nb, Ba, La, Ce) show increasing abundance

331   with decreasing MgO content for Type I RMI, except for Cr, Sc and Mn. Some of the trace

332   element data show significant scatter and no trend is recognized for MgO *vs.* Y, Nd, Sm, Eu and

333   Yb. Compositions of the RMI of this study and the crystallized MI by Klébesz et al. (2012)

334   partially overlap. However, RMI of this study show a wider compositional range. The observed

335   trends in RMI are consistent with compositional variations resulting from overheating of the MI

336   and incorporation of variable amounts of the host phase into the melt.

337   In this study, basaltic RMI define a continuous trend from Type I RMI compositions towards

338   more primitive compositions and towards the composition of the host clinopyroxene. It is

339   noteworthy that compositions of basaltic RMI always plot in between the compositions of the

340   Type I RMI, plagioclase and the host clinopyroxene (Fig. 3). This trend is more evident on the

341   Ba/Sr *vs.* 1000/Sr diagram (Fig. 3d), where mixing between end-members defines straight lines.

342   Therefore, the compositions of the basaltic RMI can be derived from the mixing of plagioclase ±

343   Type I melt ± host clinopyroxene.

344   Volatiles, including F, Cl, S, H_2O and CO_2, were analyzed in selected homogenized MI. The

345   H_2O content was uniformly low, below 0.15 wt%. The CO_2 content varied between 131-1,893

346   ppm but was mostly below 400 ppm. The F content ranged up to 4,000 ppm but in some cases it

347   is higher because the analytical conditions prevented us from determining the exact

348   concentration because the detector became saturated. The S and Cl contents also vary greatly,

15

349 reaching maximum concentrations of 156 ppm and 2,771 ppm, respectively. On one hand, no

350 correlation is observed between the volatile abundances when all types of RMI studied (basaltic-

351 RMI, Fsp-MI, High-P, and Type I) are considered, with the exception of S concentration which

352 shows a positive correlation with Cl concentration. On the other hand, we observe some

353 correlations between volatile concentrations and major and trace elements and Mg# of the

354 clinopyroxene host. For example, in Type-1 RMI, Cl increases with increasing S and H_2O.

355 Fluorine shows behavior similar to Cl with the exception of one outlier. Also, S and Cl decrease

356 with increasing Sc, and H_2O shows a strong positive correlation with MnO. Finally, there is a

357 general positive correlation between F, Cl, S, H_2O and the Mg# of the clinopyroxene host and

358 the quenching temperature (Tq).

359   Considering felspar RMI, basaltic RMI, and High-P RMI, MI show Cl vs. Zr, Rb and La

360 trends toward the origin of the axes with few outliers. Fluorine and Sbehave in a manner similar

361 to Cl. The anomalous RMI show consistent H_2O content between 0.10 and 0.20 wt% with the

362 exception of one High-P RMI that contains 0.05 wt% H_2O.

363

364 **Discussion**

365 **Comparison of the MI data with previously-published results**

366 It was previously suggested by Klébesz et al. (2012) that MI hosted in clinopyroxene from the

367 same nodule studied here record small scale heterogeneities within the melt, which is common at

368 the edges of a magma conduit system (Danyushevsky et al. 2004). However, some RMI of this

369 study that are similar to Type II MI reported by Klébesz et al. (2012) did not homogenize to a

370 glass during heating. In addition, the chemical composition of Type II MI reported by Klébesz et

371 al. (2012) and the basaltic RMI of this study show that the compositions of these MI can be

16

372 derived by mixing various proportions of melt with an An-rich feldspar and the host

373 clinopyroxene. This observation implies that basaltic RMI are overheated MI that became

374 enriched in clinopyroxene component as a result of overheating and/or the MI trapped a feldspar

375 inclusion along with the silicate melt. This interpretation is further supported by the fact that the

376 inclusion compositions are not in equilibrium with their host. In addition, RMI with anomalously

377 high Mg concentrations are usually smaller than 20 µm (Table 2 in Deposit Item-02). In order to

378 minimize H_2O loss during heating, some MI may have been heated too quickly to maintain

379 equilibrium. Therefore, if the small MI are hosted in a mineral containing larger MI that were

380 observed during the heating experiment, then the smaller MI might have homogenized at a

381 temperature that was lower than the temperature from which the crystal was quenched, and this

382 MI would have therefore been overheated. Based on these observations, we conclude that the

383 different MI compositions do not represent small scale heterogeneities, but rather that basaltic

384 RMI, feldspar RMI and high-P RMI and also Type II MI reported by Klébesz et al. (2012) all

385 trapped mineral phase(s) along with silicate melt in various proportions and which, in some

386 cases, were overheated during microthermometry. This interpretation is supported by Cl, S, and

387 F versus trace elements trends. The solid phase was often An-rich feldspar but in some cases

388 apatite was trapped with the melt, implying that clinopyroxene, apatite, An-rich feldspar and

389 melt were coexisting at the time that the MI were trapped. Therefore, it is likely that only Type I

390 RMI are representative of the melt from which the clinopyroxene crystals grew. Consequently,

391 only Type I MI compositions are compared with data from the literature to investigate the origin

392 of the nodules.

393   Compositions of MI in various host phases from nodules from different eruptions of Mt.

394 Somma-Vesuvius have been compiled from the literature (Fig. 4). Unfortunately, data are only

17

395   available for nodules from the 79 AD and younger eruptions. MI in syenite nodules and skarns

396   from the 472 AD eruption (Fulignati and Marianelli 2007; Fulignati et al. 2001) have

397   significantly different compositions than any other MI reported in the literature as well as the MI

398   of this study. Fulignati et al. (2001) interpreted nodules from the 472 AD eruption to represent

399   samples that were broken off of the magma chamber-carbonate wall rock interface and

400   transported to the surface during the eruption. In addition to the highly differentiated phonolitic

401   MI, Fulignati et al. (2001) also found complex chloride-carbonate and hydrosaline melt

402   inclusions, as well as unmixed silicate-salt melt inclusions. Compositions of MI in skarns from

403   the 1944 eruption (Fulignati et al. 2004) do not show such extreme compositions as those from

404   the 472 AD eruption, but still differ from the compositions of MI from cumulate nodules. MI

405   from skarns of the 1944 eruption tend to have lower SiO_2 and MgO content, but higher Al_2O_3,

406   MnO, Na_2O and Cl contents. In addition, hypersaline FI are commonly associated with the MI.

407   The clinopyroxene host in skarns has higher Al_2O_3 content, usually above 7 wt%, compared to

408   clinopyroxenes from the juvenile rocks (Fulignati et al. 2004). The clinopyroxene in this study

409   has significantly lower Al_2O_3 content, usually less than 6 wt%, lacks complex hydrosaline and

410   chloride-carbonate inclusions, and the RMI in this study show compositions similar to MI in

411   cumulate nodules rather than those in skarns. Consequently, the nodules studied here are not

412   thought to represent an environment near the carbonate wall rock, contrary what was previously

413   assumed (Klébesz et al. 2012). However, this does not exclude the possibility that these nodules

414   represent samples of the crystal-mush zone near the magma conduit walls.

415   Klébesz et al. (2012) concluded that the petrographic features of nodules are consistent with

416   a crystal mush origin, but it is unclear whether these nodules represent the same magma that was

417   erupted during the sustained column phase of the Sarno (PB) eruption or if they crystallized from

18

418   a melt associated with an older eruption, but were ejected later, during the Sarno eruption. In

419   order to answer this question, Type I RMI were compared to bulk rock compositions of juvenile

420   eruptive products of Mt. Somma-Vesuvius (Fig. 5).

421   Type I RMI show a continuous trend towards higher CaO/Al_2O_3 when plotted against other

422   indicators of magma evolution (Fig. 5a-e). The least magnesian Type I RMI generally fit within

423   the general trend defined by the Mt. Somma-Vesuvius rocks, whereas the Type I RMI with more

424   primitive compositions (up to about 8 wt% MgO) overlap or show a trend similar to recent

425   Vesuvius volcanics. The recent Vesuvian volcanic rocks define compositional groupings at

426   MgO> ~ 4 wt% and CaO/Al_2O_3> ~ 0.6, as has already been recognized by Danyushevsky and

427   Lima (2001) and Marianelli et al. (1999). According to their interpretations, these rocks do not

428   reflect true melt compositions, but rather represent accumulations of clinopyroxene crystals.

429   Hence, these volcanic rocks represent magmas formed by mixing of evolved melts and various

430   amounts of clinopyroxene crystals inherited from the cumulate layers (Danyushevsky and Lima

431   2001; Marianelli et al. 1999). The similarities between the trends defined by these volcanics and

432   the Type I RMI of this study support the interpretation that the observed compositional trends are

433   caused by incorporating varying proportions of clinopyroxene component into the melt due to

434   MI overheating. However, there are still some important compositional features that cannot be

435   explained by overheating.

436   As seen on plots for K_2O and MgO vs. CaO/Al_2O_3 (Fig. 5c-d), it is not possible to account

437   for the disagreement in compositions of the least MgO-rich RMI in clinopyroxene compared to

438   the whole rock trend of the Sarno (PB) and younger eruptions of the first mega-cycle by

439   overheating, regardless of the amount of clinopyroxene component added to the MI by

440   overheating. In other words, the compositions of the most representative (least MgO-rich) RMI

19

441   in this study are more enriched in MgO, K_2O, TiO_2 and P_2O_5 compared to any known

442   compositions of volcanic rocks from the Sarno (PB) eruption or any other eruptions from the

443   first mega-cycle. The same phenomenon can be observed with trace element systematics (Fig.

444   5e-g). More specifically, the compositions of MI from the nodules are more enriched in Sc, V, Cr

445   and Ni but depleted in Sr, Y, Zr, Ba and Ce compared to the bulk rock compositions of the Sarno

446   (PB) and younger volcanics of the first mega-cycle. In fact, the compositions of the least

447   magnesian RMI of this study are similar to the compositions of lava rocks from the older Somma

448   (pre-Sarno) activity. Danyushevsky and Lima (2001) reported that these pre-Sarno (PB) rocks

449   can be divided into two groups based on composition of MI hosted in clinopyroxene. The first

450   group has a composition similar to rocks of the first and second mega-cycles (low K-group),

451   while the second group shows high KO_2 and SiO_2 and low Na_2O contents (high-K group). In

452   most cases, the least magnesian compositions of MI in this study overlap with the compositions

453   of the low-K group of older Somma rocks. This overlap is best illustrated by the major elements,

454   but most of the trace elements also show similar behavior (Fig. 5). However, the concentration of

455   some of the trace elements (e.g., Y, Sm, Nd, Eu) spans a wide range and geochemical trends are

456   not well defined.

457   Despite the wide scatter of the trace element concentrations, the host clinopyroxene crystals

458   in the studied nodule are interpreted to have crystallized from a magma associated with the early

459   Somma activity, prior to the Sarno (PB) eruption, and not from the magma that was erupted

460   during the sustained column phase of the Sarno (PB) eruption. This, however, does not

461   necessarily mean that the entire nodule crystallized from the same magma. Clinopyroxene

462   composition is sensitive to changes in the conditions of crystallization, such as P, T or the melt

463   composition. The simultaneous increase in alumina and HFSE and REE with decreasing MgO is

464 characteristic of normal fractional crystallization. In addition to trends consistent with normal

465 fractionation, no zoning was observed, making it unlikely that the clinopyroxenes in the nodule

466 are xenocrysts. Therefore, the compositions of type I RMI are interpreted to represent melts

467 trapped at various stages during the formation of the nodule.

468   The origins of the skarns and cumulate nodules are well constrained, but little information is

469 available concerning the origin of sub-effusive type nodules (see above). Although the origin of

470 the nodules in this study cannot be determined with certainty, their presence in the Sarno (PB)

471 eruption indicates that the magma erupted during the Sarno (PB) eruption came from the same

472 (or deeper) magma chamber(s) that fed earlier eruptions. The ascending magma accidentally

473 entrained older, possibly already solidified, rock fragments. If the interstitial liquid had not yet

474 solidified, it would have quenched into glass, as is observed in the cumulate nodules (e.g.,

475 Hermes and Cornell 1978).

476 **Pressure and temperature of formation of the nodule**

477 One of the goals of this research was to estimate the formation conditions of the nodules, and use

478 this information to constrain the depth of magma chamber(s) during the early history of the Mt.

479 Somma-Vesuvius volcanic system. The volatile content of the melt trapped in MI is pressure

480 dependent; therefore, the volatile concentration can be used to estimate the minimum trapping

481 pressure assuming a volatile-silicate melt solubility model (e.g., Papale et al. 2006). In addition,

482 formation temperatures may also be estimated using clinopyroxene and clinopyroxene-silicate

483 melt thermobarometers.

484   The model of Papale et al. (2006) requires as input the composition of the melt, including

485 H_2O and CO_2 concentrations, temperature, and oxidation state. The model calculates the

486 pressure at which the melt would be saturated in these volatiles for the input conditions. If the

21

487   melt were volatile saturated at the time of MI trapping, then the calculated pressure indicates that

488   actual trapping pressure; if the trapped melt was volatile-undersaturated, the calculated pressure

489   represents a minimum trapping pressure. Evidence for volatile saturation was not observed in the

490   samples of the Sarno (PB) eruption (absence of FI coexisting with MI). For the calculation we

491   assumed the average composition of Type I RMI, a temperature of 1250ºC, and oxidation states

492   defined by FeO = FeO$_{tot}$*0.8 (Fig. 6). The MI showing the maximum CO_2 content suggest a

493   pressure ~300 MPa, but most of the Type I RMI show pressures between 50 and 100 MPa. It is

494   important to emphasize again that the pressures calculated represent minimum trapping pressures

495   as we observed no evidence to suggest that the MI trapped volatile-saturated melts..

496   Compositions of MI and their host clinopyroxenes were used to estimate the formation

497   conditions for the NLM1-1a nodule using the model of Putirka (2008). Putirka (2008) includes

498   the previously published models of Putirka et al. (1996, 2003) as well as newer models. As

499   discussed above, MI may have become enriched in their host clinopyroxene component as a

500   result of overheating. Published models are unable to correct for overheating, and only those MI

501   that had compositions closest to the equilibrium composition with their host were used.

502   According to Putirka (2008), one way to test for equilibrium is to compare the Fe-Mg exchange

503   coefficient [K_D(Fe-Mg)$^{cpx-liq}$] calculated from the MI and its host clinopyroxene composition to a

504   constant value of 0.28 ± 0.08 derived from 1,245 experimental observations. Because the

505   exchange coefficient can vary from 0.04-0.68, with a roughly normal distribution (Putirka 2008),

506   18 MI-host pairs where the Fe-Mg coefficient was lower than 0.40 were used here. Applying the

507   various thermobarometer models to the selected MI-host pairs, the temperature can be

508   constrained with reasonable certainty, but the pressure varies within wide ranges (Table 3). The

509   model of Putirka et al. (1996) predicted a temperature between 1043-1246 °C, with an average

510   value of 1186 °C. This same model predicts pressures of 120-1630 MPa, with an average of 610

511   MPa, and with 10 out of 18 pairs between 400-800 MPa. The accuracy of the thermobarometer

512   for a single pair is reported to be at least ± 140 MPa and ± 27 °C, and probably ± 100 MPa and ±

513   15 °C when averaged over multiple pairs (Putirka et al. 1996). The model of Putirka et al. (2003)

514   estimated temperatures of 980 to 1309 °C, with an average of 1152 °C. The estimated pressure

515   ranges from -280 to 1160 MPa, and 11 out of 18 estimates are between 600 and 1000 MPa. The

516   average estimated pressure is 760 MPa, not including the two negative pressures. The standard

517   error of the pressure estimate is 170 MPa, and for temperature the standard error is 33 K (Putirka

518   et al. 2003). Several newer thermobarometers were also developed by Putirka (2008). Most of

519   these require the input of the H_2O content of the liquid (i.e., the H_2O content of the MI). These

520   equations were not used because the H_2O content in most cases was not measured and, when it

521   was, it was very low ($\leq$0.15 wt%) and it is unclear whether it is representative or not. H_2O might

522   have been lost from the MI during the heating experiments or as a result of hydrogen diffusion

523   during the time the MI resided in the magma before eruption (e.g, Danyushevsky et al. 2002;

524   Lloyd et al. 2013; Severs et al. 2007). Considering that the duration of each heating experiment

525   was similar, the positive correlations between H_2O and Tq and Mg# of Type I RMI suggests that

526   H was significant H_2O loss did not occur during heating experiments.

527   Putirka (2008) also developed a thermobarometer based on clinopyroxene composition only.

528   A large number (212) of clinopyroxene compositions (several analyses from each crystal,

529   obtained by EPMA) were used to constrain the pressure and temperature of formation based on

530   this model. The temperature estimate is in good agreement with the results given by the

531   previously mentioned thermometers. The estimated temperature of the clinopyroxenes from this

532   study varies between 1019-1366 °C, with an average of 1184 °C. The pressure varies widely,

533   from 160 to 2480 MPa. Over half of the estimates fall between 400 and 800 MPa, with an

534   average of 780 MPa. The standard error of estimate for pressure and temperature is ± 310 MPa

535   and ± 58 °C, respectively (Putirka 2008). In summary, model calculations suggest that

536   clinopyroxene likely crystallized at slightly under 1200 °C. Unfortunately, the thermobarometer

537   models that are available do not constrain the formation pressure of the nodule with high

538   precision. Recognizing these limitations, we conclude that the NLM1-1a nodule most likely

539   formed at ≥400 MPa, corresponding to a depth of at least 11 km. This depth is consistent with a

540   minimum depth of formation calculated based on the H_2O-CO_2 contents of RMI, and this depth

541   is not improbable considering our understanding of the plumbing system of Mt. Somma-

542   Vesuvius, as described below.

543   The magma feeding system beneath Mt. Somma-Vesuvius consists of three main magma

544   storage levels, the two deepest of which are probably long-lived reservoirs (Piochi et al. 2006b).

545   Isotopic, MI and FI data (Belkin and De Vivo 1993; Belkin et al. 1985; Cioni 2000; Fulignati et

546   al. 2004; Lima et al. 2003, 2007; Marianelli et al. 1999; Piochi et al. 2006b) indicate a shallow

547   reservoir at <6 km, which typically hosts the magmas producing the plinian and sub-plinian

548   eruptions (De Vivo et al. 2010). However, Webster et al. (2012) emphasized that significant

549   concentrations of F, Cl and S can greatly influence the solubility of H_2O and CO_2; hence,

550   geobarometers based on these latter two volatile species may not adequately constrain the

551   pressure conditions, and would underestimate the equilibrium pressure. A deeper magma

552   chamber that supplies the interplinian eruptions was detected at about 8-12 km, and the deepest

553   reservoir is located at >15 km (Piochi et al. 2006b). The deep structure of the plumbing system

554   of the volcanic complex is supported by geophysical evidence as well (De Gori et al. 2001; De

555   Natale et al. 2001, 2006; Nunziata and Costanzo 2010; Nunziata et al. 2006). A low velocity

556   layer is recognized at ~15-35 km depth, which has been interpreted as the deep root for the

557   shallow crustal magma chambers (De Gori et al. 2001; De Natale et al. 2001, 2006; Nunziata et

558   al. 2006).

559   Thermobarometry results suggest that the PB-Sarno (PB) eruption was fed from magma

560   chambers that are deeper than the magma chambers that supposedly supplied the other plinian

561   eruptions (e.g., 79 AD or Avellino). This is in partial agreement with the findings of Landi et al.

562   (1999), who also predicted that a deep magma chamber fed the Sarno (PB) eruption, but from

563   slightly shallower depths of about 9-12 km. Due to the large variations in the estimated

564   pressures, it cannot be stated with certainty whether a deeper reservoir already existed beneath

565   Mt. Somma-Vesuvius prior to the Sarno (PB) eruption, or if the samples came from the same

566   reservoir that fed the main, "plinian phase" (Landi et al. 1999) of the Sarno (PB) eruption.

567

568   **Implications**

569   Mt. Somma-Vesuvius is located in a densely populated area of southern Italy, with many

570   hundreds of thousands of people living in the "red" zone surrounding the volcano (e.g., Barnes

571   2011). Even though it is currently in a dormant state, the volcano is well known for its several

572   plinian eruptions, including the infamous 79 AD eruption that destroyed Pompeii and other

573   nearby towns, and a future violent eruption cannot be excluded. Reducing uncertainty associated

574   with risk assessment requires not only continuous monitoring of the system but also a good

575   understanding of the eruption history and the evolution of the plumbing system of the volcanic

576   complex. Results presented here extend our knowledge of the geochemical conditions associated

577   with eruptions at Mt. Somma-Vesuvius to earlier eruptive events that preceded the 79 AD event,

578   and thus contribute to our understanding of the longer-term history of this volcano. Importantly,

579   our results suggest that plinian eruptions may be fed from magma sources that are deeper than is

580   generally assumed and this, in turn, has important implications for interpreting geophysical data

581   from the perspective of predicting future explosive (plinian) eruptions.

582

583   **Acknowledgements**

594

595   **References cited**

596   Anderson , A.T. (2003) An introduction to melt (glass±crystals) inclusions. In I. Samson, A.

597   Anderson, and D. Marshall, Eds., Fluid Inclusions: Analysis and Interpretation.

598   Mineralogical Association of Canada, Short Course, 32, p. 353-364.

599   Arnó, V., Principe, C., Rosi, M., Santacroce, R., Sbrana, A., and Sheridan, M.F. (1987) Eruptive

600   History. In R. Santacroce, Ed., Somma-Vesuvius. CNR Quaderni Ricerca Scientifica,

601   114, p. 53-103.

26

602 Ayuso, R.A., De Vivo, B., Rolandi, G., Seal, R.R., and Paone, A. (1998) Geochemical and

603   isotopic (Nd-Pb-Sr-O) variations bearing on the genesis of volcanic rocks from Vesuvius,

604   Italy. Journal of Volcanology and Geothermal Research, 82, 53-78.

605 Barberi, F., and Leoni, L. (1980) Metamorphic carbonate ejecta from Vesuvius plinian eruptions:

606   Evidence of the occurrence of shallow magma chambers. Bulletin Volcanologique, 43,

607   107-120.

608 Barberi, F., Bizouard, H., Clocchiatti, R., Metrich, N., Santacroce, R., and Sbrana, A. (1981) The

609   Somma-Vesuvius magma chamber: a petrological and volcanological approach. Bulletin

610   of Volcanology, 44, 295-315.

611 Barnes, K. (2011) Volcanology: Europe's ticking time bomb. Nature, 473, 140-140.

612 Belkin, H.E., and De Vivo, B. (1993) Fluid inclusion studies of ejected nodules from plinian

613   eruptions of Mt. Somma-Vesuvius. Journal of Volcanology and Geothermal Research,

614   58, 89-100.

615 Belkin, H.E., De Vivo, B., Roedder, E., and Cortini, M. (1985) Fluid inclusion geobarometry

616   from ejected Mt. Somma-Vesuvius nodules. American Mineralogist, 70, 288-303.

617 Belkin, H.E., Kilburn, C.R.J., and de Vivo, B. (1993) Sampling and major element chemistry of

618   the recent (A.D. 1631-1944) Vesuvius activity. Journal of Volcanology and Geothermal

619   Research, 58, 273-290.

620 Belkin, H.E., De Vivo, B., Török, K., and Webster, J.D. (1998) Pre-eruptive volatile content,

621   melt-inclusion chemistry, and microthermometry of interplinian Vesuvius lavas (pre-

622   A.D. 1631). Journal of Volcanology and Geothermal Research, 82, 79-95.

623 Black, S., Macdonald, R., DeVivo, B., Kilburn, C.R.J., and Rolandi, G. (1998) U-series

624   disequilibria in young (A.D. 1944) Vesuvius rocks: Preliminary implications for magma

27

625   residence times and volatile addition. Journal of Volcanology and Geothermal Research,

626   82, 97-111.

627 Bodnar, R.J., and Student, J.J. (2006) Melt inclusion in plutonic rocks: petrography and

628   microthermometry. In J.D. Webster, Ed., Melt inclusions in plutonic rocks, 36, p. 1-25.

629   Mineralogical Association of Canada.

630 Brocchini, D., Principe, C., Castradori, D., Laurenzi, M.A., and Gorla, L. (2001) Quaternary

631   evolution of the southern sector of the Campanian Plain and early Somma-Vesuvius

632   activity: insights from the Trecase 1 well. Mineralogy and Petrology, 73, 67-91.

633 Cioni, R. (2000) Volatile content and degassing processes in the AD 79 magma chamber at

634   Vesuvius (Italy). Contributions to Mineralogy and Petrology, 140, 40-54.

635 Cioni, R., Civetta, L., Marianelli, P., Metrich, N., Santacroce, R., and Sbrana, A. (1995)

636   Compositional Layering and Syn-eruptive Mixing of a Periodically Refilled Shallow

637   Magma Chamber: the AD 79 Plinian Eruption of Vesuvius. Journal of Petrology, 36,

638   739-776.

639 Cioni, R., Marianelli, P., and Santacroce, R. (1998) Thermal and compositional evolution of the

640   shallow magma chambers of Vesuvius, evidence from pyroxene phenocrysts and melt

641   inclusions. Journal of Geophysical Research, 103, 18277-18294.

642 Civetta, L., and Santacroce, R. (1992) Steady stata magma supply in the last 3400 years of

643   Vesuvius activity. Acta Vulcanologica, 2, 147-159.

644 Civetta, L., Galati, R., and Santacroce, R. (1991) Magma mixing and convective compositional

645   layering within the Vesuvius magma chamber. Bulletin of Volcanology, 53, 287-300.

646   Cortini, M., Lima, A., and De Vivo, B. (1985) Trapping temperatures of melt inclusions from

647   ejected Vesuvian mafic xenoliths. Journal of Volcanology and Geothermal Research, 26,

648   167-172.

649   Cundari, A. (1982) Petrology of clinopyroxenite ejecta from Somma-Vesuvius and their genetic

650   implications. Tschermaks mineralogische und petrographische Mitteilungen, 30, 17-35.

651   Danyushevsky, L.V., and Lima, A. (2001) Relationship between Campi Flegrei and Mt. Somma

652   volcanism: evidence from melt inclusions in clinopyroxene phenocrysts from volcanic

653   breccia xenoliths. Mineralogy and Petrology, 73, 107-119.

654   Danyushevsky, L.V., McNeill, A.W., and Sobolev, A.V. (2002) Experimental and petrological

655   studies of melt inclusions in phenocrysts from mantle-derived magmas: an overview of

656   techniques, advantages and complications. Chemical Geology, 183, 5-24.

657   Danyushevsky, L.V., Leslie, R.A.J., Crawford, A., and Durance, P. (2004) Melt Inclusions in

658   Primitive Olivine Phenocrysts: the Role of Localized Reaction Processes in the Origin of

659   Anomalous Compositions. Journal of Petrology, 45, 2531-2553.

660   De Gori, P., Cimini, G.B., Chiarabba, C., De Natale, G., Troise, C., and Deschamps, A. (2001)

661   Teleseismic tomography of the Campanian volcanic area and surrounding Apenninic belt.

662   Journal of Volcanology and Geothermal Research, 109, 55-75.

663   De Natale, G., Troise, C., Pingue, F., De Gori, P., and Chiarabba, C. (2001) Structure and

664   dynamics of the Somma-Vesuvius volcanic complex. Mineralogy and Petrology, 73, 5-

665   22.

666   De Natale, G., Troise, C., Pingue, F., Mastrolorenzo, G., and Pappalardo, L. (2006) The Somma-

667   Vesuvius volcano (Southern Italy): Structure, dynamics and hazard evaluation. Earth-

668   Science Reviews, 74, 73-111.

669   De Vivo, B., Rolandi, G., Gans, P.B., Calvert, A., Bohrson, W.A., Spera, F.J., and Belkin, H.E.

670   (2001) New constraints on the pyroclastic eruptive history of the Campanian volcanic

671   Plain (Italy). Mineralogy and Petrology, 73, 47-65.

672   De Vivo, B., Lima, A., Kamenetsky, V.S., and Danyushevsky, L.V. (2006) Fluid and melt

673   inclusions in the sub-volcanic environments from volcanic systems: Examples from the

674   Neapolitan area and Pontine Islands, Italy. Mineralogical Association of Canada Short

675   Course 36, p. 211-237, Montreal, Quebec.

676   De Vivo, B., Petrosino, P., Lima, A., Rolandi, G., and Belkin, H. (2010) Research progress in

677   volcanology in the Neapolitan area, southern Italy: a review and some alternative views.

678   Mineralogy and Petrology, 99, 1-28.

679   Del Moro, A., Fulignati, P., Marianelli, P., and Sbrana, A. (2001) Magma contamination by

680   direct wall rock interaction: constraints from xenoliths from the walls of a carbonate-

681   hosted magma chamber (Vesuvius 1944 eruption). Journal of Volcanology and

682   Geothermal Research, 112, 15-24.

683   Esposito, R., Klebesz, R., Bartoli, O., Klyukin, Y., Moncada, D., Doherty, A., and Bodnar, R.

684   (2012) Application of the Linkam TS1400XY heating stage to melt inclusion studies.

685   Central European Journal of Geosciences, 4, 208-218.

686   Esposito, R., Hunter, J., Schiffbauer, J.D., Shimizu, N., and Bodnar, R.J. (2014) An assessment

687   of the reliability of melt inclusions as recorders of the pre-eruptive volatile content of

688   magmas. American Mineralogist, 99, 976–998.

689   Fulignati, P., and Marianelli, P. (2007) Tracing volatile exsolution within the 472 AD "Pollena"

690   magma chamber of Vesuvius (Italy) from melt inclusion investigation. Journal of

691   Volcanology and Geothermal Research, 161, 289-302.

692   Fulignati, P., Marianelli, P., and Sbrana, A. (1998) New insights on the thermometamorphic-

693   metasomatic magma chamber shell of the 1944 eruption of Vesuvius. Acta

694   Vulcanologica, 10, 47-54.

695   Fulignati, P., Marianelli, P., Santacroce, R., and Sbrana, A. (2000) The skarn shell of the 1944

696   Vesuvius magma chamber. Genesis and P-T-X conditions from melt and fluid inclusion

697   data. European Journal of Mineralogy, 12, 1025-1039.

698   Fulignati, P., Kamenetsky, V.S., Marianelli, P., Sbrana, A., and Mernagh, T.P. (2001) Melt

699   inclusion record of immiscibility between silicate, hydrosaline, and carbonate melts:

700   Applications to skarn genesis at Mount Vesuvius. Geology, 29, 1043-1046.

701   Fulignati, P., Marianelli, P., Santacroce, R., and Sbrana, A. (2004) Probing the Vesuvius magma

702   chamber-host rock interface through xenoliths. Geological Magazine, 141, 417-428.

703   Fulignati, P., Kamenetsky, V.S., Marianelli, P., and Sbrana, A. (2005) Fluid inclusion evidence

704   of second immiscibility within magmatic fluids (79 AD eruption of Mt. Vesuvius).

705   Periodico di Mineralogia, 74, 43-54.

706   Gilg, H.A., Lima, A., Somma, R., Belkin, H.E., De Vivo, B., and Ayuso, R.A. (2001) Isotope

707   geochemistry and fluid inclusion study of skarns from Vesuvius. Mineralogy and

708   Petrology, 73, 145-176.

709   Helo, C., Longpre, M.A., Shimizu, N., Clague, D.A., and Stix, J. (2011) Explosive eruptions at

710   mid-ocean ridges driven by CO_2-richmagmas. Nature Geoscience, 4, 260-263.

711   Hermes, O.D., and Cornell, W.C. (1978) Petrochemical significance of xenolithic nodules

712   associated with potash-rich lavas of Somma-Vesuvius volcano, NSF final technical

713   report, p. 58, University of Rhode Island.

714   -. (1981) Quenched crystal mush and associated magma compositions as indicated by

715   intercumulus glasses from Mt. Vesuvius, Italy. Journal of Volcanology and Geothermal

716   Research, 9, 133-149.

717   Hermes, O.D., and Cornell, W.C. (1983) The significance of mafic nodules in the ultra-potassic

718   rocks from central Italy - reply. Journal of Volcanology and Geothermal Research, 16,

719   166-172.

720   Joron, J.L., Metrich, N., Rosi, M., Santacroce, R., and Sbrana, A. (1987) Chemistry and

721   Petrography In R. Santacroce, Ed., Somma-Vesuvius. CNR Quad. Ric. Sci. , 114, p. 105-

722   174, Roma.

723   Klébesz, R., Bodnar, R., De Vivo, B., Török, K., Lima, A., and Petrosino, P. (2012) Composition

724   and origin of nodules from the ≈20 ka Pomici di Base (PB)-Sarno eruption of Mt.

725   Somma-Vesuvius, Italy. Central European Journal of Geosciences, 4, 324-337.

726   Landi, P., Bertagnini, A., and Rosi, M. (1999) Chemical zoning and crystallization mechanisms

727   in the magma chamber of the Pomici di Base plinian eruption of Somma-Vesuvius

728   (Italy). Contributions to Mineralogy and Petrology, 135, 179-197.

729   Le Bas, M.J., Le Maitre, R.W., Streckeisen, A., and Zanettin, B. (1986) A chemical classification

730   of volcanic rocks based on the total alkali-silica diagram. Journal of Petrology, 27, 745-

731   750.

732   Lima, A., Belkin, H.E., and Török, K. (1999) Understanding Vesuvius magmatic processes:

733   evidence from primitive silicate-melt inclusions in medieval scoria clinopyroxenes

734   (Terzigno Formation). Mineralogy and Petrology, 65, 185-206.

735   Lima, A., Danyushevsky, L.V., De Vivo, B., and Fedele, L. (2003) A model for the evolution of

736   the Mt. Somma-Vesuvius magmatic system based on fluid and melt inclusion

737   investigations. In B. De Vivo and R.J. Bodnar, Eds., Melt Inclusions in Volcanic

738   Systems: Methods, Applications, Problems. Developments in Volcanology, 5, p. 227-

739   249. Elsevier Press, Amsterdam.

740 Lima, A., De Vivo, B., Fedele, L., Sintoni, F., and Milia, A. (2007) Geochemical variations

741   between the 79 AD and 1944 AD Somma-Vesuvius volcanic products: Constraints on the

742   evolution of the hydrothermal system based on fluid and melt inclusions. Chemical

743   Geology, 237, 401-417.

744 Lloyd, A., Plank, T., Ruprecht, P., Hauri, E., and Rose, W. (2013) Volatile loss from melt

745   inclusions in pyroclasts of differing sizes. Contributions to Mineralogy and Petrology,

746   165, 129-153.

747 Longerich, H.P., Jackson, S.E., and Gunther, D. (1996) Inter-laboratory note. Laser ablation

748   inductively coupled plasma mass spectrometric transient signal data acquisition and

749   analyte concentration calculation. Journal of Analytical Atomic Spectrometry, 11, 899-

750   904.

751 Lowenstern, J.B. (2003) Melt Inclusions Come of Age: Volatiles, Volcanoes and Sorby's

752   Legacy. In B. De Vivo and R.J. Bodnar, Eds., Melt Iclusions in Volcanic Systems:

753   Methods, Applications, Problems. Development in Volcanology, 5, p. 1-22. Elsevier

754   Press, Amsterdam.

755 Marianelli, P., Metrich, N., Santacroce, R., and Sbrana, A. (1995) Mafic magma batches at

756   Vesuvius: a glass inclusion approach to the modalities of feeding stratovolcanoes.

757   Contributions to Mineralogy and Petrology, 120, 159-169.

758 Marianelli, P., Métrich, N., and Sbrana, A. (1999) Shallow and deep reservoirs involved in

759   magma supply of the 1944 eruption of Vesuvius. Bulletin of Volcanology, 61, 48-63.

33

760   Marianelli, P., Sbrana, A., Métrich, N., and Cecchetti, A. (2005) The deep feeding system of

761   Vesuvius involved in recent violent strombolian eruptions. Geophysical Research Letters,

762   32, L02306.

763   Marini, L., Chiappini, V., Cioni, R., Cortecci, G., Dinelli, E., Principe, C., and Ferrara, G. (1998)

764   Effect of degassing on sulfur contents and $\delta^{34}S$ values in Somma-Vesuvius magmas.

765   Bulletin of Volcanology, 60, 187-194.

766   Mastrolorenzo, G., Munno, R., and Rolandi, G. (1993) Vesuvius 1906: a case study of

767   paroxymal eruption and its relation to eruption cycles. Journal of Volcanology and

768   Geothermal Research, 58, 217-237.

769   Mues-Schumacher, U. (1994) Chemical variation of the A.D. 79 pumice deposits of Vesuvius.

770   European Journal of Mineralogy, 6, 387-395.

771   Nunziata, C., and Costanzo, M. (2010) Low VS crustal zones in the Campanian Plain (Southern

772   Italy). Mineralogy and Petrology, 100, 215-225.

773   Nunziata, C., Natale, M., Luongo, G., and F. Panza, G. (2006) Magma reservoir at Mt. Vesuvius:

774   Size of the hot, partially molten, crust material detected deeper than 8 km. Earth and

775   Planetary Science Letters, 242, 51-57.

776   Paone, A. (2006) The geochemical evolution of the Mt. Somma-Vesuvius volcano. Mineralogy

777   and Petrology, 87, 53-80.

778   Paone, A. (2008) Fractional crystallization models and B–Be–Li systematics at Mt Somma-

779   Vesuvius volcano (Southern Italy). International Journal of Earth Sciences, 97, 635-650.

780   Papale, P., Moretti, R., and Barbato, D. (2006) The compositional dependence of the saturation

781   surface of $H_2O + CO_2$ fluids in silicate melts. Chemical Geology, 229, 78-95.

34

782 Piochi, M., Ayuso, R.A., De Vivo, B., and Somma, R. (2006a) Crustal contamination and crystal

783   entrapment during polybaric magma evolution at Mt. Somma-Vesuvius volcano, Italy:

784   Geochemical and Sr isotope evidence. Lithos, 86, 303-329.

785 Piochi, M., De Vivo, B., and Ayuso, R.A. (2006b) The magma feeding system of Somma-

786   Vesuvius (Italy) strato-volcano: new inferences from a review of geochemical and Sr,

787   Nd, Pb and O isotope data. In B. De Vivo, Ed., Volcanism in the Campania Plain:

788   Vesuvius, Campi Flegrei and Ignimbrites, p. Chapter 9: 181-202. Elsevier B. V.

789 Putirka, K. (2008) Thermometers and Barometers for Volcanic Systems. In K. Putirka and F.J.

790   Tepley III, Eds., Minerals, inclusions and volcanic processes, Reviews in Mineralogy &

791   Geochemistry, 69, p. 61-120. Mineralogical Society of America.

792 Putirka, K., Johnson, M.C., Kinzler, R., and Walker, D. (1996) Thermobarometry of mafic

793   igneous rocks based on clinopyroxene-liquid equilibria, 0-30 kbar. Contributions to

794   Mineralogy and Petrology, 123, 92-108.

795 Putirka, K.D., Mikaelian, H., Ryerson, F., and Shaw, H. (2003) New clinopyroxene-liquid

796   thermobarometers for mafic, evolved, and volatile-bearing lava compositions, with

797   applications to lavas from Tibet and the Snake River Plain, Idaho. American

798   Mineralogist, 88, 1542-1554.

799 Raia, F., Webster, J.D., and De Vivo, B. (2000) Pre-eruptive volatile contents of Vesuvius

800   magmas: constraints on eruptive history and behavior. I - The medieval and modern

801   interplinian activities. European Journal of Mineralogy, 12, 179-193.

802 Roedder, E. (1979) Origin and significance of magmatic inclusions. Bulletin de Mineralogie,

803   102, 487-510.

804   Rolandi, G. (1997) The eruptive history of Somma-Vesuvius. In M. Cortini and B. De Vivo,

805   Eds., Volcanism and Archeology in Mediterranean Area. Reserch Signpost, p. 77-88.

806   Trivandrum.

807   Rolandi, G., Barrella, A.M., and Borrelli, A. (1993) The 1631 eruption of Vesuvius. Journal of

808   Volcanology and Geothermal Research, 58, 183-201.

809   Rolandi, G., Bellucci, F., Heizler, M.T., Belkin, H.E., and De Vivo, B. (2003) Tectonic controls

810   on the genesis of ignimbrites from the Campanian Volcanic Zone, southern Italy.

811   Mineralogy and Petrology, 79, 3-31.

812   Rosi, M., and Santacroce, R. (1983) The 472 A.D. 'Pollena' eruption: volcanological and

813   petrological data for this poorly known plinian-type event at Vesuvius. Journal of

814   Volcanology and Geothermal Research, 17, 249-271.

815   Santacroce, R. (1987) Somma-Vesuvius. CNR Quaderni della Ricerca Scientifica 114, 8, p. 251.

816   Santacroce, R., Bertagnini, A., Civetta, L., Landi, P., and Sbrana, A. (1993) Eruptive dynamics

817   and petrogenetic processes in a very shallow magma reservoir: The 1906 eruption of

818   Vesuvius. Journal of Petrology, 34, 383-425.

819   Santacroce, R., Cioni, R., Marianelli, P., Sbrana, A., Sulpizio, R., Zanchetta, G., Donahue, D.J.,

820   and Joron, J.L. (2008) Age and whole rock-glass compositions of proximal pyroclastics

821   from the major explosive eruptions of Somma-Vesuvius: A review as a tool for distal

822   tephrostratigraphy. Journal of Volcanology and Geothermal Research, 177, 1-18.

823   Savelli, C. (1968) The problem of rock assimilation by Somma-Vesuvius magma. Contributions

824   to Mineralogy and Petrology, 18, 43-64.

825   Schiano, P., Clocchiatti, R., Ottolini, L., and Sbrana, A. (2004) The relationship between

826   potassic, calc-alkaline and Na-alkaline magmatism in South Italy volcanoes: A melt

827   inclusion approach. Earth and Planetary Science Letters, 220, 121-137.

828   Severs, M.J., Azbej, T., Thomas, J.B., Mandeville, C.W., and Bodnar, R.J. (2007) Experimental

829   determination of H_2O loss from melt inclusions during laboratory heating: Evidence from

830   Raman spectroscopy. Chemical Geology, 237, 358-371.

831   Sobolev, V.S., and Kostyuk, V.P. (1975) Magmatic crystallization based on a study of melt

832   inclusions. "Nauka" Press (in Russian; translated in part in Fluid Inclusion Research, 9,

833   182-253), Novosibirsk.

834   Somma, R., Ayuso, R.A., De Vivo, B., and Rolandi, G. (2001) Major, trace element and isotope

835   geochemistry (Sr-Nd-Pb) of interplinian magmas from Mt. Somma-Vesuvius (Southern

836   Italy). Mineralogy and Petrology, 73, 121-143.

837   Sorby, H.C. (1858) On the Microscopical, Structure of Crystals, indicating the Origin of

838   Minerals and Rocks. Quarterly Journal of the Geological Society, 14, 453-500,.

839   Thomas, J.B., and Bodnar, R.J. (2002) A technique for mounting and polishing melt inclusions

840   in small (<1mm) crystals. American Mineralogist, 87, 1505-1508.

841   Vaggelli, G., De Vivo, B., and Trigila, R. (1993) Silicate-melt inclusions in recent Vesuvius

842   lavas (1631-1944): II. Analytical chemistry. Journal of Volcanology and Geothermal

843   Research, 58, 367-376.

844   Varekamp, J.C. (1983) The significance of mafic nodules in the ultra-potassic rocks from central

845   Italy - discussion. Journal of Volcanology and Geothermal Research, 16, 161-165.

846   Villemant, B., Trigila, R., and DeVivo, B. (1993) Geochemistry of Vesuvius volcanics during

847   1631–1944 period. Journal of Volcanology and Geothermal Research, 58, 291-313.

848   Washington. (1906) The roman comagmatic Region. 199 p. Carnegie Inst Washington Publ. No.

849   57.

850   Webster, J.D., Raia, F., De Vivo, B., and Rolandi, G. (2001) The behavior of chlorine and sulfur

851   during differentiation of the Mt. Somma-Vesuvius magmatic system. Mineralogy and

852   Petrology, 73, 177-200.

853   Webster, J.D., Goldoff, B., Sintoni, F., and De Vivo, B. (2012) Solubilities of H-O-C-S-Cl

854   volatiles in fluids and silicate melts and their control on magmatic processes.

855   Mineralogical Magazine, 76, 2532.

856   Zambonini, F. (1910) Mineralogia Vesuviana. Atti delle Reale Accademia delle Scienze Fisiche

857   e Matematiche di Napoli, Ser. 2°, 14, 1-463.

858

859   **Figure Captions**

860   **Figure 1.** Variation diagrams of representative major and trace elements in clinopyroxene from

861   nodule NLM1-1a from the Sarno (Pomici di Base) eruption of Mt. Somma-Vesuvius (Italy). a)

862   Spider diagram of clinopyroxene compositions normalized to primitive mantle. Trace element

863   concentrations determined by LA-ICP-MS. b) Cr vs MgO, c) CaO/Al_2O_3 vs. MgO, and d) Al_2O_3

864   vs, MgO. Error bars in panels b), c), and d) indicate the average standard deviations. Major

865   element concentrations of panels b), c), and d) were determined by EPMA, Cr was determined

866   by LA-ICP-MS.

867   **Figure 2**. Composition of MI hosted in clinopyroxene from sample NLM1-1a plotted on the total

868   alkali silica diagram (Le Bas et al. 1986). All data recalculated to 100% anhydrous. Average

869   estimated standard deviation is smaller than the size of the symbols. Data were obtained by

870   EPMA. Grey fields represent MI data from Klébesz et al. (2012).

38

871 **Figure 3.** Composition of MI hosted in clinopyroxene from sample NLM1-1a. a) MgO vs. CaO,

872 b) MgO vs. TiO_2, c) MgO vs. La, d) 1000/Sr vs. Ba/Sr. Dashed lines indicate mixing between

873 end-members. Error bars on panels b) and c) indicate the average standard deviation. All data

874 recalculated to 100% anhydrous. Major and minor element concentrations of panels a), b) and c)

875 were determined by EPMA, trace element concentrations of panel d) by LA-ICP-MS.

876 **Figure 4.** Comparisons between the compositions of Type I RMI (this sudy) and compositions of

877 MI in skarn and cumulate nodules from the literature (Fulignati and Marianelli 2007; Fulignati et

878 al. 2001, 2004; Hermes and Cornell 1981; Lima et al. 2003, 2007). a) CaO/Al_2O_3 vs. MnO, b)

879 CaO/Al_2O_3 vs. MgO, c) CaO/Al_2O_3 vs. SiO_2. Error bars indicate the average standard deviation.

880 All data recalculated to 100 % anhydrous. MI data representative of skarn and cumulate nodules

881 from Mt. Somma-Vesuvius are shown by grey fields. Data of this study were obtained by

882 EPMA.

883 **Figure 5.** Comparison of compositions of Type I RMI in clinopyroxene from sample NLM1-1a

884 with bulk rock compositions of juvenile eruptive rocks from Mt. Somma-Vesuvius. a)

885 CaO/Al_2O_3 vs. SiO_2, b) CaO/Al_2O_3 vs. Na_2O, c) CaO/Al_2O_3 vs. K_2O, d) CaO/Al_2O_3 vs. MgO, e)

886 CaO/Al_2O_3 vs. Ba, f) and g) K_2O/Ba vs. Sr/Zr. Bulk rock data, indicated by grey fields, are from

887 the literature (see text). All data recalculated to 100% anhydrous. Average estimated standard

888 deviations are smaller than the size of the symbols. On panel g) full, dashed and dotted lines

889 indicate the compositional trend of the bulk rocks of the third, second and first mega-cycles,

890 respectively. Major and minor element concentrations were determined by EPMA, trace element

891 concentrations by LA-ICP-MS.

892 **Figure 6.** H_2O-CO_2 systematics of RMI from this study. The isobars were calculated using the

893 H_2O-CO_2-silicate melt solubility model by Papale et al. (2006). For the calculation, we assumed

39

894 the average composition of Type I RMI for the melt, a temperature of 1250ºC, and redox

895 conditions controlled by FeO = FeO_{tot}*0.8. Note that the maximum pressure estimated for Type I

896 RMI plots close to the 300 MPa isobar. This pressure is considered a minimum trapping pressure

897 due to the effect of overheating and absence of volatile saturation. Error bars indicate the average

898 standard deviation. Volatile compositions were obtained by SIMS.

899

Table 1. Representative analyses of clinopyroxene from sample NLM1-1a

Sample:	cpx165	cpx153	cpx151	cpx143 (B)	cpx143 (C)	cpx140	cpx110	cpx05	cpx117	cpx116	cpx159	cpx139	cpx150
SiO_2	49.98(17)	48.00(17)	50.63(20)	49.46(20)	51.08(20)	49.12(26)	50.89(20)	49.85(20)	49.84(20)	49.81(20)	49.76(17)	50.38(20)	48.28(20)
TiO_2	1.10(3)	1.22(3)	0.93(3)	1.18(3)	0.89(3)	1.51(5)	0.75(2)	0.76(2)	1.10(3)	1.03(3)	1.18(3)	1.33(3)	1.61(4)
Al_2O_3	4.90(5)	5.07(5)	4.63(5)	6.11(6)	3.91(5)	6.37(8)	3.84(4)	4.72(5)	4.47(5)	4.49(5)	4.79(5)	5.45(6)	6.40(6)
FeO	7.61(13)	8.15(13)	6.59(12)	7.03(12)	6.59(12)	8.32(19)	6.66(12)	6.38(11)	7.94(14)	7.92(14)	7.55(13)	7.63(13)	8.11(13)
MnO	0.20(3)	0.15(3)	0.16(3)	0.20(4)	0.17(3)	0.16(5)	0.17(3)	0.12(3)	0.13(3)	0.22(4)	0.20(4)	0.19(3)	0.18(4)
MgO	14.09(10)	13.87(10)	14.53(10)	13.80(9)	14.73(10)	13.18(13)	15.12(11)	14.77(11)	13.99(10)	14.13(10)	13.95(10)	13.86(10)	12.93(9)
CaO	22.05(12)	21.05(12)	21.85(11)	21.65(11)	22.23(11)	21.31(15)	22.40(12)	22.74(12)	22.04(12)	22.08(12)	21.48(12)	21.83(11)	21.70(11)
Na_2O	0.36(2)	0.38(2)	0.32(2)	0.32(2)	0.28(2)	0.44(4)	0.26(2)	0.25(2)	0.33(2)	0.34(2)	0.33(2)	0.35(2)	0.35(2)
Total	100.37	97.97	99.70	100.00	100.12	100.46	100.21	99.79	99.87	100.09	99.26	101.12	99.66
Sc	126(155)	104(160)	109(163)	119(161)	116(163)	125(163)	123(144)	116(132)	126(141)	126(155)	108(164)	117(159)	138(191)
V	461(8)	455(10)	396(11)	373(10)	430(10)	483(10)	449(10)	448(8)	493(8)	353(9)	389(11)	435(9)	507(12)
Cr	699(7)	252(9)	1203(10)	604(9)	456(9)	381(8)	1025(8)	291(7)	190(8)	651(7)	209(9)	541(8)	878(10)
Ni	81(4)	97(4)	93(4)	72(4)	102(4)	100(4)	107(4)	86(4)	82(4)	85(5)	86(4)	94(4)	77(4)
Rb	-	-	-	-	-	-	-	-	-	1.7(28.1)	-	-	-
Sr	92(2)	92(2)	84(2)	83(3)	93(3)	93(2)	88(2)	110(2)	94(2)	83(3)	85(3)	89(3)	90(3)
Y	28.5(2.7)	34.8(2.8)	18.8(2.9)	27.3(3.8)	23.0(3.8)	40.4(2.9)	24.9(2.5)	36.9(2.0)	41.3(2.3)	29.6(3.5)	29.0(3.5)	30.0(2.8)	34.3(2.8)
Zr	91(2)	93(2)	52(2)	79(2)	62(2)	138(2)	70(3)	101(1)	120(2)	83(1)	80(2)	85(1)	120(1)
Nb	0.4(4.5)	0.5(4.9)	-	0.4(5.4)	0.2(5.4)	0.5(5.0)	0.3(4.0)	0.6(3.4)	0.5(3.8)	0.6(3.8)	0.4(4.6)	0.4(4.8)	0.5(5.7)
Ba	0.4(2.0)	1.0(2.0)	0.2(1.4)	4.7(1.5)	0.2(1.5)	0.6(1.6)	0.5(1.5)	8.9(1.4)	0.4(1.6)	1.0(1.6)	0.2(2.4)	0.3(1.9)	0.4(1.6)
La	8.7(1.2)	8.7(2.5)	5.4(3.1)	7.3(2.4)	6.6(2.4)	11.3(1.8)	6.9(1.9)	13.5(1.1)	11.5(1.7)	7.6(2.9)	7.8(1.8)	8.4(2.5)	10.4(2.1)
Ce	30.6(0.8)	33.1(1.6)	20.9(1.9)	26.7(1.9)	21.9(1.9)	37.8(1.3)	23.8(1.2)	42.4(1.0)	39.1(1.1)	26.0(1.3)	28.5(1.5)	30.9(1.6)	37.5(2.4)
Nd	30.7(2.5)	32.7(2.4)	20.9(2.5)	27.2(2.8)	22.3(2.8)	40.7(2.7)	23.8(2.4)	40.4(1.7)	41.1(1.7)	28.2(2.8)	27.9(2.1)	31.4(2.9)	37.9(2.9)
Sm	9.5(1.5)	10.0(1.9)	5.8(1.6)	8.7(2.3)	6.8(2.3)	11.7(2.0)	7.5(1.1)	11.9(1.2)	12.0(0.9)	8.8(1.4)	9.0(1.1)	10.0(1.9)	10.4(1.6)
Eu	2.0(1.4)	2.2(1.3)	1.2(1.9)	2.0(2.2)	1.7(2.3)	2.7(1.8)	1.8(2.1)	2.6(1.4)	2.9(1.9)	1.8(1.9)	2.1(1.3)	2.1(2.1)	2.5(2.3)
Yb	2.2(1.2)	2.7(1.7)	1.4(1.6)	2.2(1.8)	1.4(1.9)	3.0(1.6)	2.0(0.9)	3.1(1.0)	3.4(1.2)	2.6(1.4)	1.9(1.9)	2.9(1.0)	2.9(1.2)
mg#	0.82	0.83	0.82	0.80	0.82	0.77	0.86	0.88	0.81	0.83	0.79	0.78	0.78
En	41	41	43	41	43	40	43	42	41	41	41	41	39
Wo	46	45	46	47	46	46	46	47	46	46	46	46	47
Fs	13	14	11	12	11	14	11	10	13	13	13	13	14

mg# = Mg/(Mg+Fe^{2+}); En, Wo, Fs, enstatite, wollastonite, ferrosilite in mol% of clinopyroxene; -, below detection limit; major and minor elements are in wt%, trace elements are in ppm. Major and minor elements were determined by EPMA, trace elements by LA-ICP-MS. Estimated standard deviation (e.s.d.) is indicated in parentheses.

Table 2. Composition of representative RMI in clinopyroxene

	Fsp or fsp-bearing MI			Basaltic RMI						High-P RMI		
Sample	cpx134p2_A	cpx157_A	Sample	cpx05_A2	cpx901_A	cpx116_B	cpx05_C	cpx123p1_B	Sample	cpx129_A	cpx118p1_D	cpx129_C
SiO_2	48.55(24)	50.40(24)	SiO_2	48.61(24)	50.30(25)	47.23(23)	46.33(23)	51.24(24)	SiO_2	39.17(19)	43.76(22)	44.07(22)
TiO_2	0.10(3)	0.11(3)	TiO_2	0.95(4)	0.67(3)	1.21(5)	1.93(8)	0.87(4)	TiO_2	1.04(4)	1.40(5)	1.14(4)
Al_2O_3	32.26(19)	29.40(11)	Al_2O_3	14.07(12)	16.88(15)	10.54(9)	11.78(10)	12.63(12)	Al_2O_3	6.01(5)	8.63(8)	10.25(9)
FeO	0.71(7)	0.92(7)	FeO	6.71(17)	5.56(14)	8.46(21)	9.73(24)	6.07(16)	FeO	7.46(18)	8.30(20)	7.40(18)
MnO	-	0.03(4)	MnO	0.24(10)	0.06(3)	0.18(8)	0.26(11)	0.12(4)	MnO	0.25(10)	0.21(9)	0.25(11)
MgO	0.04(2)	0.04(2)	MgO	7.55(11)	6.43(10)	11.36(17)	9.51(14)	8.52(10)	MgO	9.24(14)	10.47(15)	9.49(14)
CaO	16.42(14)	13.56(12)	CaO	16.32(18)	14.82(16)	19.20(21)	16.48(18)	15.74(13)	CaO	25.69(28)	18.57(20)	21.52(24)
Na_2O	1.84(6)	3.18(8)	Na_2O	1.30(4)	1.52(5)	1.18(4)	1.41(4)	2.04(7)	Na_2O	0.82(3)	2.27(7)	1.06(3)
K_2O	0.44(3)	0.37(2)	K_2O	1.77(3)	2.88(5)	0.92(2)	1.54(3)	0.89(3)	K_2O	0.38(1)	0.49(1)	0.75(1)
P_2O_5	0.08(4)	0.05(4)	P_2O_5	0.47(5)	0.49(5)	0.04(0)	0.17(2)	1.07(9)	P_2O_5	8.26(82)	5.29(53)	3.88(38)
Total	100.44	98.06	Total	97.98	99.60	100.32	99.15	99.18	Total	98.32	99.39	99.80
Ab	16	29	CaO/Na_2O	13	10	16	12	8	CaO/Na_2O	31	8	20
An	81	69	(CaO/Na_2O)corr						(CaO/Na_2O)cor	13	3	5
Or	3	2	Sc	73(239)	56(323)	52(178)	65(267)		Sc	109(338)	96(268)	79(320)
Sc	-	-	V	326(14)	255(20)	323(10)	533(15)		V	465(22)	469(17)	409(21)
V	-	-	Cr	62(11)	63(16)	540(8)	109(13)		Cr	248(19)	325(12)	198(18)
Cr	-	-	Ni	62(7)	72(7)	73(5)	54(7)		Ni	76(11)	-	-
Ni	-	141(6)	Rb	69(40)	70(49)	90(32)	57(42)		Rb	-	12(44)	14(49)
Rb	-	-	Sr	726(4)	1005(5)	319(3)	464(4)		Sr	200(5)	163(4)	638(4)
Sr	1752(5)	1393(4)	Y	23.8(5.6)	15.4(5.7)	21.9(4.0)	28.7(4.1)		Y	51.4(5.7)	41.9(5.8)	59.9(5.4)
Y	-	-	Zr	99(2)	70(3)	83(2)	94(3)		Zr	131(3)	130(2)	116(3)
Zr	-	-	Nb	6.9(7.0)	5.7(10.2)	22.8(4.4)	37.6(6.9)		Nb	2.4(9.5)	4.9(8.0)	2.7(8.9)
Nb	-	-	Ba	778(3)	1542(3)	279(2)	499(3)		Ba	58(3)	138(2)	389(3)
Ba	439(3)	145(3)	La	19.9(2.2)	13.2(3.7)	10.4(3.4)	15.7(2.2)		La	55.6(4.5)	17.2(2.2)	74.1(4.3)
La	5.3(3.7)	7.5(4.4)	Ce	44.8(2.1)	31.2(3.0)	32.1(1.4)	43.4(2.0)		Ce	127.9(2.2)	52.8(1.7)	169.1(2.1)
Ce	7.6(2.9)	21.3(1.9)	Nd	34.8(2.6)	23.6(5.7)	20.4(3.2)	39.3(3.5)		Nd	98.6(5.9)	42.4(4.3)	105.0(5.5)
Nd	-	6.9(3.4)	Sm	7.5(2.7)	8.2(3.4)	10.2(1.6)	6.7(2.4)		Sm	20.1(4.0)	14.9(2.6)	23.6(3.8)
Sm	-	-	Eu	2.5(2.1)	1.6(3.2)	1.5(2.2)	1.8(2.8)		Eu	4.7(4.0)	3.2(3.0)	5.9(3.7)
Eu	-	-	Yb	1.7(1.3)	-	2.0(1.7)	3.6(2.0)		Yb	3.6(2.5)	2.7(1.4)	4.2(2.4)
Yb	-	-	CO_2	1717 ± 240	283 ± 40			362 ± 51	CO_2	179 ± 25		
			H_2O	0.15 ± 0.01	0.14 ± 0.01			0.04 ± 0.00	H_2O	0.12 ± 0.01		
			F	980 ± 49	482 ± 24			350 ± 17	F	768 ± 38		
			S	103 ± 6	47 ± 3			31 ± 2	S	41 ± 2		
			Cl	652 ± 156	513 ± 123			129 ± 31	Cl	350 ± 84		
			Tq	1256		1251	1256	1250	Tq	1241	1245	1241
			host mg#	0.82	0.83	0.85	0.85	0.82	host mg#	0.85	0.88	0.83

(continued)

Table 2. Composition of representative RMI in clinopyroxene (continued)

Sample	Type I RMI												
	cpx165_B	cpx153_E	cpx151_D	cpx143_B	cpx143_C	cpx140_D	cpx110_B	cpx05_B	cpx117_A	cpx116_A	cpx159_A	cpx139_C	cpx150_A
SiO_2	49.99(24)	52.31(24)	53.98(27)	50.14(26)	52.39(27)	52.32(27)	52.43(26)	51.57(26)	51.78(26)	48.74(24)	50.77(24)	52.50(27)	51.97(27)
TiO_2	1.29(5)	1.11(4)	0.93(4)	1.20(4)	1.04(4)	1.31(5)	0.98(4)	1.19(5)	1.39(5)	1.37(5)	1.34(5)	1.21(5)	1.32(5)
Al_2O3	11.80(11)	15.17(13)	15.66(13)	13.03(12)	15.43(13)	15.65(13)	11.99(11)	11.80(10)	16.14(14)	14.08(12)	14.70(13)	12.87(12)	15.39(13)
FeO	7.85(18)	6.91(17)	5.38(15)	7.02(17)	6.12(16)	7.37(18)	6.66(16)	8.39(21)	8.43(21)	12.27(30)	8.67(19)	7.05(17)	7.10(17)
MnO	0.11(5)	0.09(5)	0.08(4)	0.13(4)	0.10(5)	0.13(5)	0.21(9)	0.22(9)	0.18(7)	0.16(7)	0.14(4)	0.12(5)	0.09(4)
MgO	7.90(10)	4.21(7)	5.24(8)	8.04(10)	4.88(8)	4.56(8)	8.43(12)	8.35(12)	4.35(6)	5.39(8)	5.03(8)	7.09(9)	4.81(8)
CaO	13.30(12)	6.63(9)	8.03(10)	12.82(12)	8.43(10)	8.00(9)	13.10(14)	13.85(15)	8.49(9)	9.77(11)	8.32(10)	12.18(12)	7.22(9)
Na_2O	1.76(6)	3.02(8)	2.27(7)	1.85(6)	2.15(7)	2.77(8)	1.74(5)	1.53(5)	2.62(8)	2.65(8)	2.67(8)	2.13(7)	3.18(8)
K_2O	3.53(6)	6.65(9)	6.57(9)	4.21(7)	6.52(9)	6.09(8)	3.85(6)	3.47(6)	5.24(9)	4.14(7)	5.65(8)	4.00(7)	6.21(8)
P_2O_5	0.68(7)	0.72(7)	0.73(8)	0.66(7)	0.83(8)	0.98(8)	0.72(7)	0.37(4)	0.74(7)	0.72(7)	0.80(8)	0.57(7)	0.89(8)
Total	98.22	96.82	98.85	99.10	97.87	99.18	100.12	100.73	99.34	99.30	98.10	99.72	98.18
CaO/Na_2O	8	2	4	7	4	3	8	9	3	4	3	6	2
Sc	74(186)	-	-	-	-	-	53(208)	55(371)	45(215)	75(254)	-	70(151)	-
V	336(10)	262(24)	342(29)	332(13)	301(13)	302(18)	275(14)	371(21)	251(12)	371(15)	316(18)	322(9)	306(20)
Cr	224(9)	46(21)	547(26)	331(11)	140(11)	59(15)	130(11)	151(18)	25(12)	505(12)	57(15)	210(8)	67(15)
Ni	78(5)	-	-	-	84(5)	-	67(5)	-	62(7)	-	201(7)	59(4)	-
Rb	126(51)	232(112)	62(287)	180(117)	229(120)	167(180)	219(33)	135(59)	237(33)	72(46)	125(74)	168(84)	218(172)
Sr	405(2)	544(5)	289(6)	374(4)	576(4)	582(4)	510(3)	452(6)	544(3)	282(5)	388(5)	386(3)	500(4)
Y	27.1(3.2)	20.8(6.7)	28.7(7.7)	24.4(4.8)	18.0(4.9)	27.3(5.3)	22.8(3.5)	35.4(5.7)	23.7(3.5)	31.9(5.7)	41.5(5.9)	27.5(2.7)	20.0(4.5)
Zr	173(2)	188(4)	111(7)	187(3)	174(3)	238(4)	133(4)	161(4)	190(3)	144(2)	265(3)	174(1)	229(2)
Nb	25.0(5.4)	40.6(11.8)	11.1(16.6)	27.7(6.8)	38.5(7.0)	44.4(9.2)	18.9(5.8)	22.8(9.6)	37.2(5.8)	18.2(6.2)	27.4(7.7)	24.4(4.6)	40.6(9.1)
Ba	1292(2)	2076(5)	660(4)	1265(2)	2115(2)	2095(3)	1464(2)	1271(4)	1967(2)	822(3)	1246(4)	1356(2)	2052(3)
La	34.0(1.4)	45.3(6.1)	19.2(8.5)	32.8(3.0)	41.6(3.1)	52.1(3.3)	33.6(2.8)	41.2(3.1)	51.8(2.6)	25.1(4.8)	41.0(3.0)	35.3(2.4)	49.4(3.4)
Ce	74.6(1.0)	85.3(3.8)	46.1(5.1)	72.4(2.4)	74.4(2.4)	100.4(2.3)	71.2(1.7)	76.2(2.8)	97.6(1.6)	62.1(2.0)	85.3(2.6)	71.7(1.5)	89.2(3.9)
Nd	41.6(3.0)	40.0(5.8)	31.2(6.8)	37.8(3.5)	33.4(3.6)	45.5(4.9)	38.1(3.5)	37.2(4.8)	46.7(2.7)	43.5(4.5)	54.5(3.6)	38.3(2.8)	41.4(4.6)
Sm	8.8(1.8)	9.9(4.5)	-	7.2(2.9)	4.8(3.1)	7.7(3.6)	8.0(1.6)	14.2(3.3)	8.6(1.4)	10.1(2.3)	9.0(1.8)	9.0(1.8)	10.6(2.6)
Eu	2.5(1.7)	3.1(3.2)	-	2.2(2.8)	1.8(2.9)	2.6(3.3)	1.9(3.1)	2.5(3.9)	2.4(2.9)	2.6(3.1)	3.9(2.1)	2.2(2.0)	1.5(3.6)
Yb	2.2(1.4)	-	-	-		2.1(3.0)	1.7(1.3)	4.5(2.8)	1.8(1.8)	2.3(2.4)	-	2.4(0.9)	2.8(2.0)
CO_2	382 ± 53	295 ± 41	220 ± 31		266 ± 37	297 ± 42	220 ± 31	268 ± 38	497 ± 70	216 ± 30	645 ± 90		272 ± 38
H_2O	0.07 ± 0.00	0.04 ± 0.00	0.04 ± 0.00		0.05 ± 0.00	0.05 ± 0.00	0.08 ± 0.00	0.12 ± 0.01	0.19 ± 0.01	0.14 ± 0.01	0.08 ± 0.00		0.04 ± 0.00
F	1951 ± 98		1364 ± 68					2211 ± 111	914 ± 46	4262 ± 213	1812 ± 91		
S	70 ± 4	100 ± 6	49 ± 3		77 ± 5	106 ± 6	155 ± 9	132 ± 8	150 ± 9	129 ± 8	111 ± 7		101 ± 6
Cl	647 ± 155	686 ± 165	547 ± 131		872 ± 209	912 ± 219	2546 ± 611	1185 ± 284	2226 ± 534	1710 ± 410	903 ± 217		843 ± 202
Tq	1229	1225	1224	1241	1241	1233	1255	1256	1240	1251	1224	1243	1213
host mg#	0.82	0.83	0.82	0.80	0.82	0.77	0.86	0.88	0.81	0.83	0.79	0.78	0.78

mg# = Mg/(Mg+Fe^{2+}); Ab,An, Or, albite, anorthite and orthoclase in mol% of feldspar; -, below detection limit; (CaO/Na$_2$O)corr, CaO/Na$_2$O ratio after subtracting apatite; Tq, quenching temperature;host mg#, mg# of the host clinopyroxene; major and minor elements and H2O are in wt%, all others in ppm. Major and minor elements were determined by EPMA, trace elements by LA-ICP-MS, volatile elements by SIMS. Estimated standard deviation (e.s.d.) is indicated in parentheses. In case of SIMS analyses, the estimate of the measurement error is shown.

Table 3. Predicted formation conditions of clinopyroxene calculated by different geothermobarometers

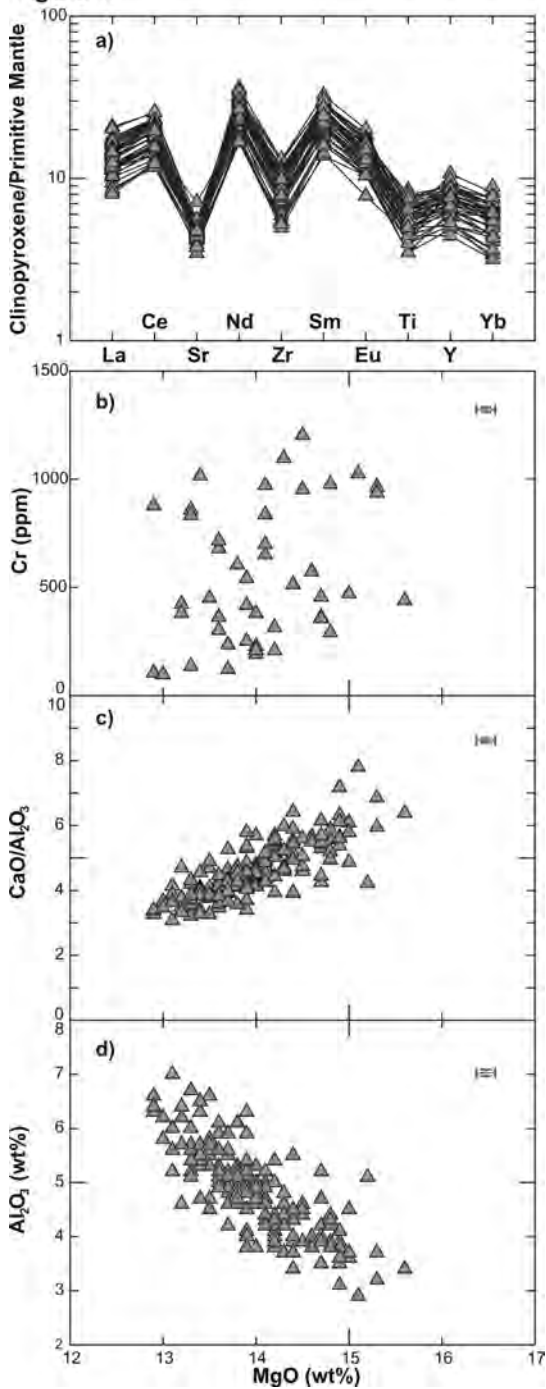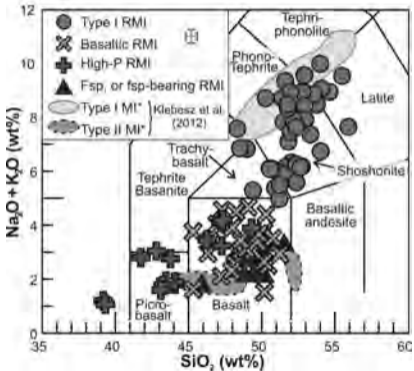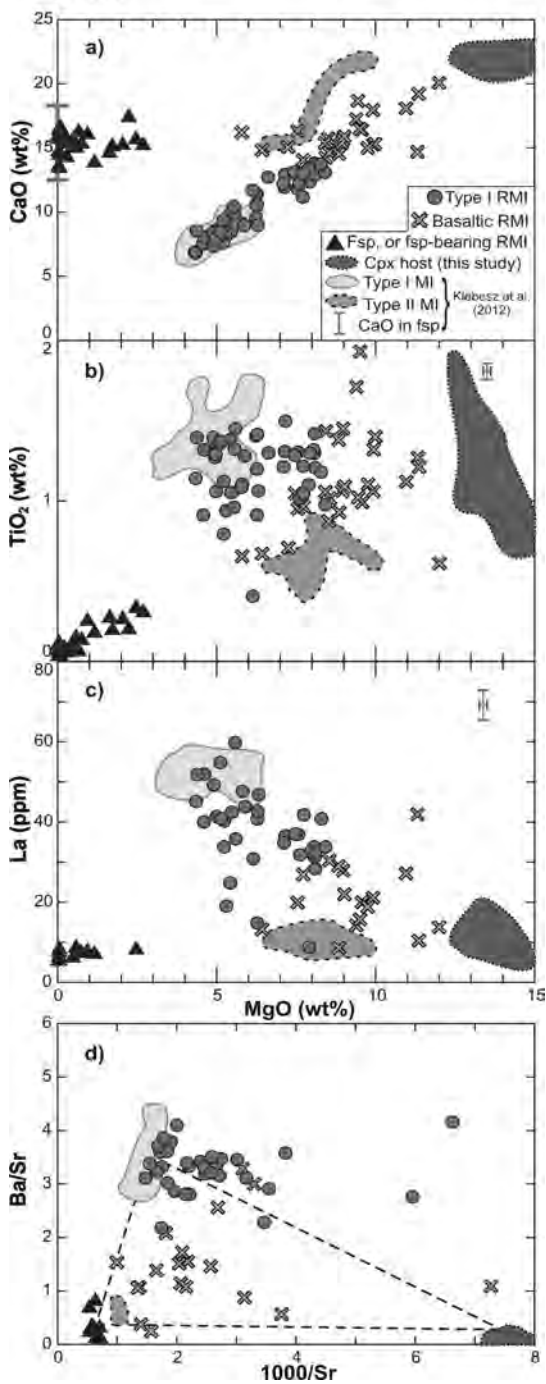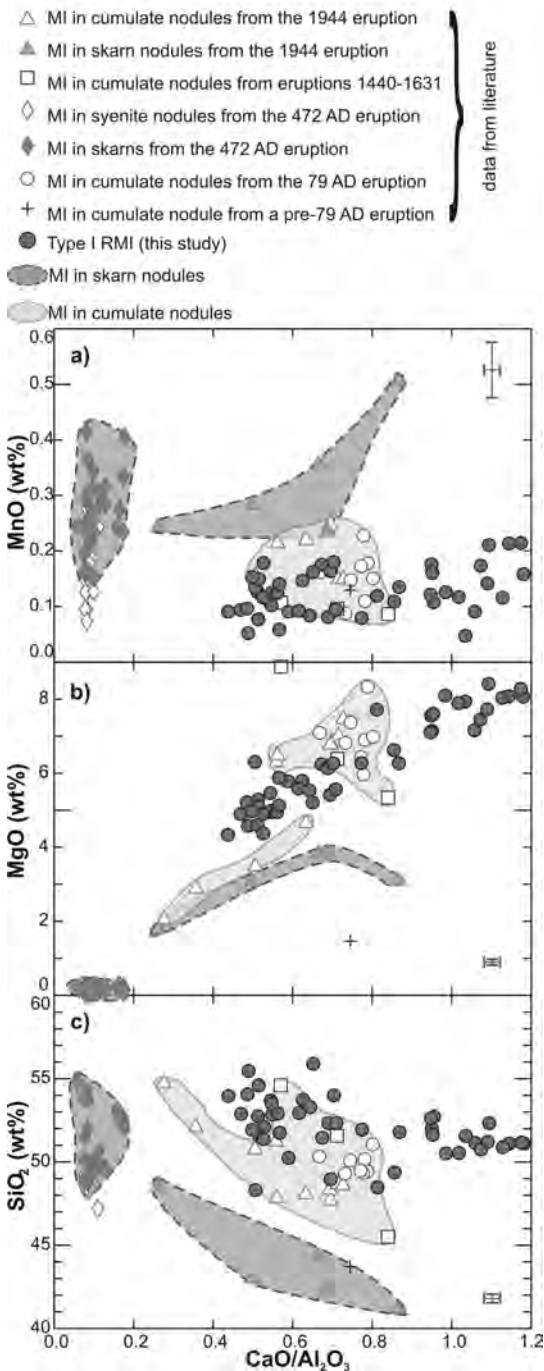|	Putirka et al. (1996)	Putirka et al. (2003)	Putirka (2008)
T	1043-1246 °C ± 27 °C	980-1309 °C ± 33 °C	1019-1366 °C ± 58 °C
T *average*	1186 °C ± 15 °C	1152 °C ± 33 °C	1184 °C ± 58 °C
Pressure	120-1630 MPa ± 100 MPa	-280-1160 MPa ± 170 Mpa	160-2480 kMPa ± 310 Mpa

Figure 1.

Figure 2.

Figure 3.

Figure 4.

△ MI in cumulate nodules from the 1944 eruption
▲ MI in skarn nodules from the 1944 eruption
□ MI in cumulate nodules from eruptions 1440-1631
◇ MI in syenite nodules from the 472 AD eruption
◈ MI in skarns from the 472 AD eruption
○ MI in cumulate nodules from the 79 AD eruption
+ MI in cumulate nodule from a pre-79 AD eruption
● Type I RMI (this study)
▨ MI in skarn nodules
▨ MI in cumulate nodules

data from literature

a) MnO (wt%)

b) MgO (wt%)

c) SiO$_2$ (wt%)

CaO/Al$_2$O$_3$

Figure 5.

Figure 6.

Figure 6.

Legend:
- ▲ Fsp. or fsp-bearing RMI
- ● Type I RMI
- ✕ Basaltic RMI
- ✦ High-P RMI

Y-axis: CO_2 (ppm), from 0 to 3000
X-axis: H_2O (wt%), from 0.00 to 0.30

Isobar lines: 300 MPa, 200 MPa, 100 MPa, 50 MPa